1-31-2019 10:00 AM

Analyzing myocardial R2* mapping pre- and post-myocardial infarction in a canine model

Khalid Abdalla, *The University of Western Ontario*

Supervisor: Dr. Donna Goldhawk, *Lawson Research Institute*
Co-Supervisor: Dr. Neil Gelman, *Lawson Research Institute*
A thesis submitted in partial fulfillment of the requirements for the Master of Science degree in Medical Biophysics
© Khalid Abdalla 2019

Abstract

Myocardial hemorrhage (MH) may occur following myocardial infarction (MI). Myocardial hemorrhage can be assessed by image-based measurements of R2* (1/T2*) which are sensitive to iron-based byproducts of hemorrhage. However, automated detection of MH throughout the entire left ventricle (LV) is challenging due to R2* contributions from magnetic field distortions (susceptibility artifact). To provide insight for improved MH detection, we analyzed canine cardiac magnetic resonance images that had previously been acquired at baseline and several time points (3 to 41 days) following experimentally induced MI. The images were processed to generate R2* maps and cardiac polar plots. A baseline composite polar plot was generated to identify a large LV region (~ 75% of LV) with relatively low and uniform R2* (suggesting low susceptibility artifact). The probability distribution of R2* values on the cumulative and individual polar plots was analyzed to provide insight for future development of automated analysis of MH. Also, the boundaries of this uniform region were used to define the region over which post-MI polar plots were analyzed. A threshold (0.08 ms^{-1}) to differentiate abnormally high R2* regions from normal R2* regions was determined from baseline polar plots. The mean R2* values of normal regions in the post-MI images remained approximately constant as a function of time post-MI and close to the mean R2* from baseline images. The mean R2* values of abnormal regions appeared to peak at day 3 post-MI but remained elevated compared to the remote region (0.04 ms^{-1}): day 3 (0.11 ms^{-1}, $p < 0.001$), day 7, 15, 21 and 41 (0.08 ms^{-1}, $p < 0.05$). At all post-MI times investigated, these data suggest that hemorrhage and its byproducts remained for several weeks.

Keywords

Acknowledgments

First, I am grateful for my God (Allah) for everything in my life. Who does not thank God does not thank people. I would love to express my faithful thanks to my thesis supervisors, Dr. Donna Goldhawk, and Dr. Neil Gelman. The doors to Dr. Goldhawk and Dr. Gelman offices were always open whenever I faced trouble in my research or writing. They consistently steered me in the right path whenever they thought I needed it.

I would also like to thank my committee advisors, Dr. Frank Prato, and Dr. Jonathan Thiessen, for their advice and insightful comments regarding my work. Also, I am grateful to Dr. Terry Thompson for being our lab's collaborator. My sincere gratitude also goes to the Goldhawk lab's members for their help with my study. Specifically, I would like to thank Daisy Sun, Sarah Donnelly, and Tian Hou and Praveen Dassanayake. Special thanks for my colleague Farzad Asadi for his help. I would also like to acknowledge Heather Biernaski and John Butler, for their technical assistance during this project.

Last but not least, I would like to thank my family. First is a special thanks to my wife, Areej Al-Saad, who always encouraged me to move forward in my education and career. Also, I am so grateful to my own family especially my children, Lammar, Hamzah, Mohammad, and my lovely Miayar. I would also like to thank my extended family members, in particular, my mother, for her all prayers for me, my sisters and brothers. God bless my father.

Table of Contents

List of Abbreviations

AAR	Area At Risk
AHA	American Heart Association
CMR	Cardiac Magnetic Resonance
ECG	Electrocardiogram
GRE	Gradient Echo
LA	Left Atrium
LAD	Left Anterior Descending Artery
LCA	Left Coronary Artery
LCX	Left Circumflex Artery
LV	Left Ventricle
MI	Myocardial Infarction
RA	Right Atrium
RCA	Right Coronary Artery
RV	Right Ventricle
SD	Standard Deviation
SI	Signal Intensity
SNR	Signal-to-Noise Ratio
TE	Echo Time
TR	Repetition Time
T2*W	T2* weighted image

List of Figures

List of Tables

1   Introduction

Myocardial infarction (MI) is a common manifestation of heart disease and mortality. In 2012-13, approximately 2.4 million Canadian adults aged 20 years or older were diagnosed with heart disease, including 578,000 with a history of MI [1].

Occlusion of one or several of the heart's coronary arteries may cause MI and one of the pathophysiological complications occurring post-MI is myocardial hemorrhage. However, since its identification in the early 1960s, the pathophysiology of myocardial hemorrhage is still unclear. A large amount of hemorrhage can lead to severe inflammation and influence the healing process. Detection of myocardial hemorrhage using noninvasive methods such as magnetic resonance imaging (MRI) would be beneficial for precise risk stratification and potential therapeutic strategies.

Assessment of the myocardial T2* relaxation rate has been shown to add relevant information. Signal below the normal range of myocardial T2* (<20 ms) is associated with a significant decrease in left ventricle (LV) ejection fraction [2]. However, a reliable assessment of myocardial T2*-weighted images of the entire LV post-MI is challenging due to image artifacts and the presence of edema. In addition, manual delineation of the hypointense zone is prone to observer errors [3]. Furthermore, myocardial T2* mapping post-MI in most previous studies was performed at 1.5 Tesla (T); whereas, conceptually, myocardial mapping at 3 T is interesting due to improved signal at higher field strength which contributes enhanced signal to noise ratio (SNR). Also, the relaxation rate 1/T2* associated with iron-related contrast (such as hemorrhage) increases with field strength. In this thesis, we examined myocardial T2* at 3 T in a canine MI model using a T2* mapping technique. The studies include animals with no injury and animals studied at various time points (3 to 41 days) post MI.

In this thesis chapter, we will provide an introduction to the heart and the pathophysiology of MI, including a discussion on myocardial hemorrhage, utilization of cardiac magnetic resonance (CMR) in myocardial hemorrhage, and state-of-the-art mapping methods.

1.1   The heart

The long axis of the heart in the body is oriented obliquely relative to the long axis of the body. The superior portion of the heart is called the base, which is connected to the vena cava, aorta, pulmonary arteries and veins. The inferior part of the heart, located above the diaphragm, is called the apex.

The heart comprises four chambers: the upper chambers are the right atrium (RA) and left atrium (LA); the lower chambers are the right ventricle (RV) and left ventricle (LV) (Figure 1.1). The right and left side of the heart work synchronously. Blood enters the right side of the heart and is sent to the lungs. Oxygenated blood is passed to the left side of the heart and pumped out to the body. In humans, the heartbeat ranges from 60 to 100 beats per minute, at rest. Adequate and stable circulation of blood is ensured by the myocardium and may be affected by injuries, such as MI, that cause abnormal cardiac function.
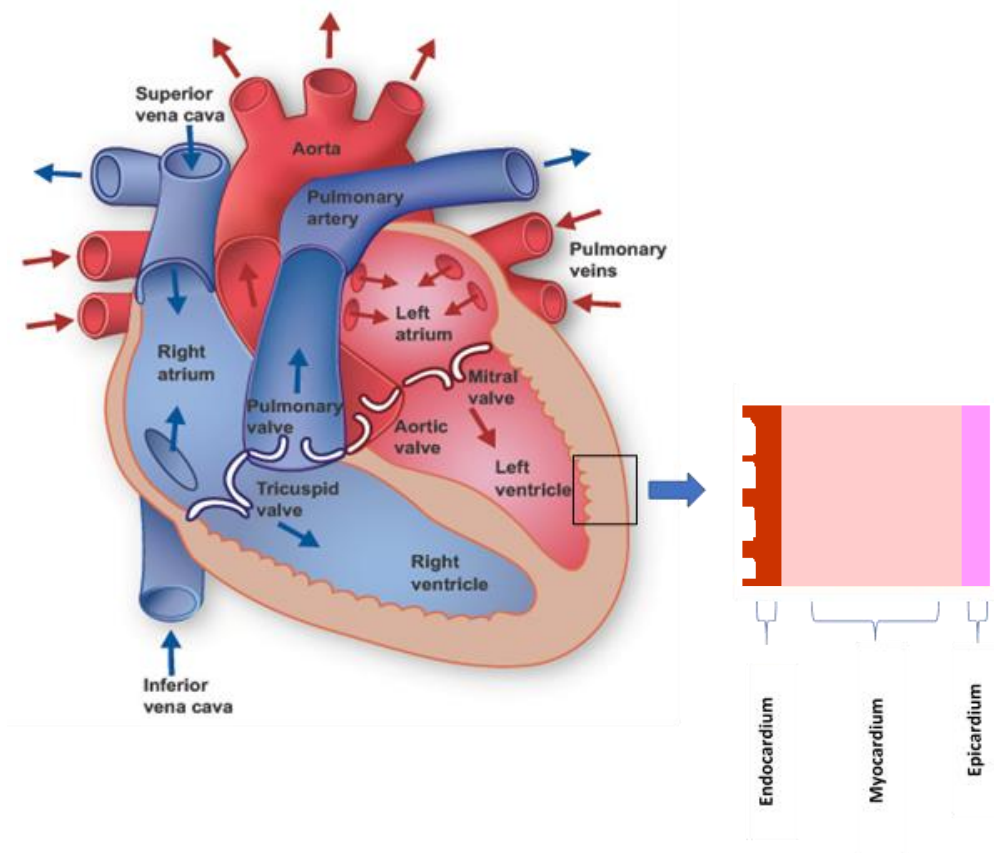
Figure 1. 1. Anatomy of the heart. The diagram indicates the four chambers of the heart; left atrium (LA), left ventricle (LV), right atrium (RA), and right ventricle (RV). The oxygen-poor blood flows from the RA to the RV through the tricuspid valve (blue arrows). The oxygen-rich blood flows from the LA to the LV through the mitral valve (red arrow). The wall of the heart includes three layers: Epicardium, Myocardium, and Endocardium. The diagram was extracted from the Texas Heart Institute website with permission from Texas Heart Institute [4].

Cells of the heart tissue may be grouped into two major categories: myocytes and non-myocytes. Myocytes form ~70-80% of the myocardial volume. Non-myocytes include immune cells, endothelial cells, and fibroblasts. All components of the heart participate in cardiac function and seem to be involved in the response to myocardial injury. While myocytes are the main contributors to contractile activity, they may also play a central role in cardiac dysfunction [5, 6].

As a circulatory pump, the heart gets its nutrients from the coronary arteries. There are four major coronary arteries: the left coronary artery (LCA) and the right coronary artery (RCA). The LCA is divided into two branches: the circumflex artery (LCX) which supplies blood to the lateral and back side of the LV, and the left anterior descending artery (LAD) which supplies the frontal side of the septum in addition to the bottom and front side of the LV. The RCA supplies the right ventricle (Figure 1.2). Disorders of the coronary arteries have severe implications because they limit the blood supply to the heart, causing myocardial ischemia and necrosis. In severe cases, the myocardial infarction may then evolve to heart failure.

The canine heart has a well-developed system of collateral vessels which is an important similarity to the human heart. However, there are several species differences. A canine heart has various pulmonary veins, varying from 4 to 8 while the human heart has only 4 or 5 pulmonary veins. At rest, an adult dog's heartbeat ranges from 60 to 160 beats per minute, varying more widely compared to the human heart rate (60-100 beats per minute). Additional differences involve the positioning of the vena cava and slight variations in the shapes and sizes of the atrial appendages [7, 8].
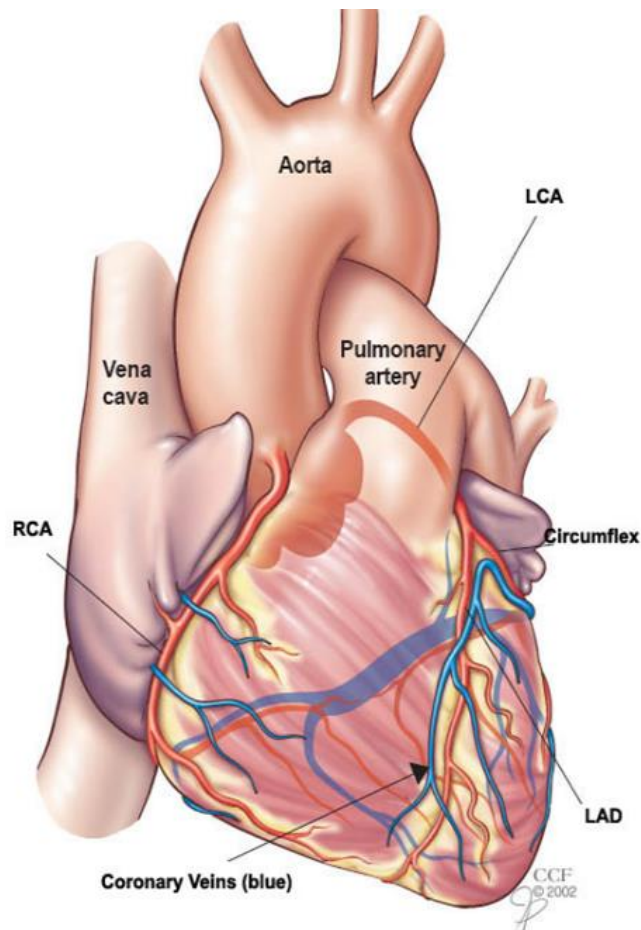
Figure 1. 2. Coronary arteries of the heart. The diagram indicates the four coronary arteries: : left anterior descending (LAD), left circumflex (LCX), left coronary artery (LCA), and right coronary artery (RCA). The diagram was extracted from the Texas Heart Institute website with permission from Texas Heart Institute [9].

1.2   Myocardial infarction

Myocardial infarction can be classified based on anatomical and clinical diagnostic criteria. From an anatomic point of view, MI is categorized as either transmural or nontransmural. A transmural MI, also called a full-wall thickness MI, results in ischemic necrosis extending from the endocardium (inner wall) through the myocardium to the epicardium (outer wall) of the LV (Figure 1.1). A nontransmural MI corresponds to ischemic necrosis that does not spread through the full thickness of the myocardium. The least perfused zones of the heart, which are at the highest risk of ischemia, are the endocardial and subendocardial regions [10].

Clinically, an electrocardiogram (ECG) is used to monitor electrical variations in the heart. At rest, cardiac cells are polarized, resulting in a difference in electrical potential across their membranes. When they depolarize, the ECG records the sequence of waves that correlate with electrical impulses during each heartbeat. In a normal recording, the waves are labeled P, Q, R, S, and T. The P wave represents atrial depolarization. During this process, the two atria are contracting. The QRS wave represents ventricular depolarization, causing ventricular contraction. Atrial repolarization and relaxation take place after the P wave and is found within the QRS complex because ventricles tend to contract more strongly than atria. The T wave represents ventricular repolarization when the ventricles are relaxing. Changes in the waveforms and distances among the waves can be used clinically to estimate the severity of MI. For example, based on electrocardiographic findings, an ST-elevation myocardial infarction (STEMI) is caused by sudden complete blockage of a coronary artery (LAD or RCA). A severely narrowed artery which is not completely blocked usually creates a non-ST-elevation myocardial infarction (NSTEMI). However, this classification does not distinguish transmural from nontransmural MI [11].

1.2.1   Pathophysiology of MI

The primary cause of MI is a build-up of atherosclerotic plaque(s) in the coronary artery. A rupture in the plaque forms a thrombus which in turn reduces the flow of blood to the heart muscle, causing ischemia. This creates a partial or complete decrease in oxygen to the area depending on that vascular supply and also necrosis, which is the death of myocardial cells or tissue [12]. In animal studies, MI can be created by direct occlusion of either the LAD or LCX by ligation of the artery. Studies in a canine MI model showed that the evolution of cell death (myocyte necrosis) with time progressed as a wave front, starting at the endocardium and extending to the epicardium. The area at risk (AAR) is defined as the myocardial area distal from the occlusion distal from the occlusion [13]. The experimental model used in this thesis is described in section 2.1.2.

Experimentally, the minimum time for inducing a small MI is in the range of 20-30 minutes. The relationship between infarct size and duration of the occlusion is not linear [14]. Studies have compared 40 versus 90 minutes of coronary artery occlusion, which produced infarct sizes of 16% and 32%, respectively, while 24 hours of occlusion induced an infarct size involving 45% of the AAR [15, 16]. Furthermore, small deviations in the position of the coronary artery occlusion can lead to large differences in the infarct size. While studying MI in anesthetized animals failed to prove that infarct size was affected by myocardial demand, infarct size was related to myocardial demand in the conscious state [17–19].

1.2.2   Pathophysiological responses post-MI

Restoration of coronary artery perfusion to the ischemic myocardial region is the most critical process for limiting ventricular arrhythmias, infarct size and risk of heart failure [20]. However, reperfusion injury may be an adverse outcome of the process since it has been correlated with worsening or progression of ischemic damage. This leads to apoptosis and stunning (brief cardiac dysfunction due to ischemia) as well as reperfusion arrhythmias, and irreversible injury [21].

Edema is also associated with ischemia-reperfusion in MI and occurs because of an inflammatory reaction. Endothelial leakiness causes swelling of tissue and results in excessive fluid, plasma protein leakage and changes in osmotic pressure in the ischemic region [22]. Microvascular obstruction (MVO), also referred to as a no-reflow phenomenon, results from blockage of the myocardial microcirculation (in vessels less than 200 μm in diameter). MVO is associated with poor patient outcome and adverse left ventricular remodeling [23]. Furthermore, severe microvascular injury coupled with reperfusion may result in myocardial hemorrhage, defined as the extravasation of erythrocytes (red blood cells) through severely damaged endothelial walls [24]. Myocardial hemorrhage is associated with left ventricular systolic dysfunction [25], adverse remodeling representing changes in the heart size and function [26, 27] and poor clinical outcomes [28].

The histological findings of early studies by Kolner *et al.* [29], in a canine MI model, showed that myocardial hemorrhage was located in the core of the infarcted region. Subsequent experimental analyses have presented additional insight into the pathophysiology of endothelial injury and myocardial hemorrhage. Through coronary artery occlusion, the cardiovascular endothelium undergoes hypoxia and high shear stress. The hypoxic environment promotes the production of cytokines and growth factors which influence vascular leakage and increase vascular permeability. As a result, the endothelial wall becomes vulnerable and eventually necrotic [30–32].

Despite the increased risk of myocardial hemorrhage with continued periods of ischemia, this condition, apart from reperfusion, does not lead to myocardial hemorrhage. Occlusion alone will cause intracellular swelling of the endothelial cells and myocytes, while reperfusion is attributed with inducing myocardial hemorrhage [33, 34]. During the extravasation of red blood cells from the endothelium into the myocardium, edema forms and restricts the healing process [35]. However, Kali *et al.* (2016) [36] showed that iron deposition appeared in permanent occlusion MI (non-reperfused).

1.3   Utilization of cardiac MRI in myocardial hemorrhage

Cardiovascular magnetic resonance (CMR) imaging has achieved clinical importance in the noninvasive evaluation of myocardial viability and function post-MI, allowing for high-resolution assessment of the infarct size. A hypointense core within the infarcted myocardium in T2-weighted and T2*-weighted CMR has been correlated with the presence of hemorrhagic infarcts [37, 38]. The breakdown products of hemoglobin are paramagnetic substances and hence contribute to shortening of T2* relaxation times. Thus, CMR is considered a powerful technique for post-MI assessments. Its growing use in clinical care assists clinicians to establish an accurate diagnosis and aides in therapeutic decision making.

1.3.1   Basic concepts of MRI

The MRI signal utilized to produce images is either from water or fat within the tissue. Certain nuclear species including the hydrogen nucleus have a property known as nuclear spin ($\mathbf{S}$). These nuclei also have an associated magnetic moment ($\boldsymbol{\mu}$) due to a spinning charge (e.g., proton) which is related to the spin by

$$\boldsymbol{\mu} = \gamma\,\mathbf{S} \qquad\qquad (1.1)$$

where γ is known as the gyromagnetic ratio. Normally, the magnetic moment vectors are orientated randomly. To detect the MRI signal, these nuclei are subjected to a static magnetic field ($\mathbf{B_0}$), where the direction of $\mathbf{B_0}$ defines the direction of the z-axis of the coordinate system used in MRI. In this situation, the z-components of magnetic moments ($\boldsymbol{\mu}$) of the nuclei will either align parallel (low energy state) or anti-parallel (high energy state) to the direction of $\mathbf{B_0}$. This realignment occurs over a time period of several times longer than the T1 relaxation time (defined below) which is typically of the order of a few to several seconds. A greater proportion of these magnetic moments aligns parallel to $\mathbf{B_0}$ than antiparallel, leading to a net proton nuclear magnetization vector ($\mathbf{M_0}$) in the direction of $\mathbf{B_0}$ where the proton nuclear magnetization is the vector sum of all proton magnetic moments per unit volume. Also, the magnetic moments precess around the direction of $\mathbf{B_0}$

(Figure 1.3), with an angular frequency known as the Larmor frequency (ω_0) and described by

$$\omega_0 = \gamma\, B_0 \qquad\qquad (1.2)$$

where γ is the gyromagnetic ratio of the nucleus ($\gamma/2\pi = 42.58$ MHz/T for hydrogen (^{1}H)), and B_0 is the primary magnetic field in Tesla (T).
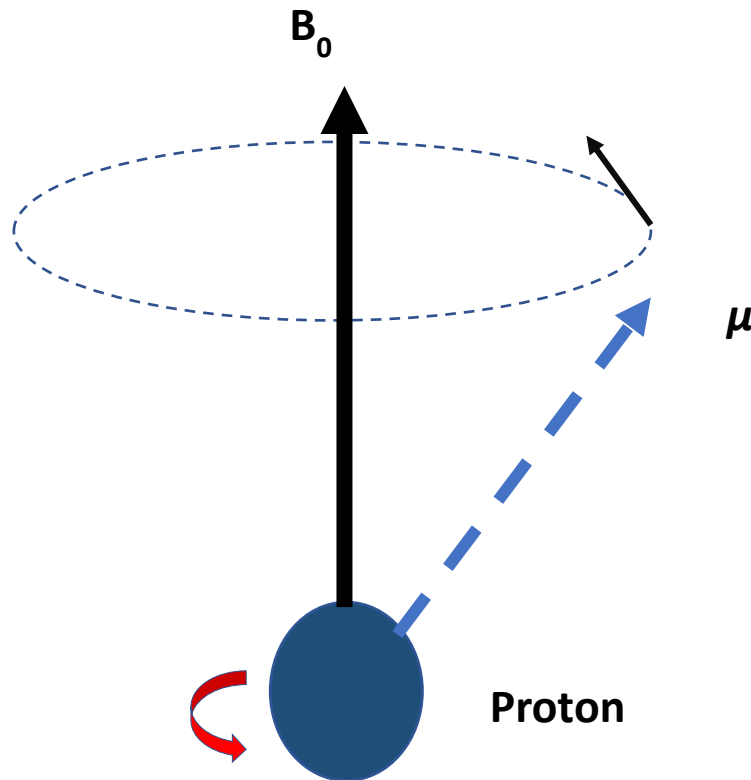
Figure 1. 3. Larmor frequency. The rotation of the axis of spin (blue dashed arrow) of the nucleus around the direction of B_0 is called precession. The small red arrow designates the nuclear spin and the precession is designated by the small black arrow.

The frequency of precession is called Larmor frequency and depends on the strength of B_0.

When a time-dependent magnetic field (**B₁**) in the form of a short pulse is applied at ω_0, it results in a disturbance of the spin alignment. Some low energy parallel spins flip to high energy states, decreasing longitudinal magnetization. As a result, the net magnetization vector (**M₀**) turns towards the transverse plane (perpendicular to **B₀**), producing a transverse magnetization (**M$_{xy}$**).

When **B1** is switched off, a portion of the protons flips back to the low energy state, losing their kinetic energy to the surrounding nuclei. until thermal equilibrium is achieved and the magnetization returns its initial value parallel to **B₀**. This process is known as longitudinal relaxation or spin-lattice relaxation. The longitudinal relaxation time (*T1*) is the time required for **M$_z$** to reach 63% of its equilibrium value (**M₀**).

$$\mathbf{M_z}\,(t) = \mathbf{M_0}\,(1\text{-}e^{-t/T1}) \qquad\qquad (1.3)$$

The equation above assumes that **M$_z$** = 0 at t =0. Variations in *T1* among tissues is utilized to generate signal contrast on MR images.

Proton magnetic moments that were in phase start to dephase due to the variation of the Larmor frequency between nuclei. This is called spin-spin relaxation and results in a reduction in **M$_{xy}$** according to

$$\mathbf{M_{xy}} = \mathbf{M_0}\,e^{-t/T2} \qquad\qquad (1.4)$$

where *T2* is the time required for M_{xy} to decay to approximately 37% of its initial value. Transverse relaxation happens more quickly than longitudinal relaxation and is due to mechanisms related to the dephasing process among spins. Spatial variations in the magnetic field experienced by protons cause spatial variation in **ω₀** throughout the tissue. On a microscopic scale, the random spatial variations are generated by the presence of adjacent nuclei, which generate weak magnetic fields. Also, dephasing occurs due to the exchange of energy between nuclei. These processes result in *T2* relaxation.

On a macroscopic scale, even if the applied **B₀** is considered perfectly homogeneous, variations in magnetic susceptibilities of various biological materials create spatial variation in the magnetic field experienced by protons. Paramagnetic (or superparamagnetic) particles, like iron-containing byproducts of hemorrhage, have positive susceptibility and generate substantial variation in the magnetic field. Other biological substances, such as hemoglobin in red blood cells and ferritin in tissue, are paramagnetic and accelerate spin dephasing.

The majority of biological substances are diamagnetic. The variations in diamagnetism at air-tissue interfaces leads to distortion of the magnetic field. These air-tissue interferences are associated with the heart-lung interface and air pockets in the colon, bowel, and stomach. This leads to macroscopic variation in the magnetic field which contributes to T2* and is known as a (magnetic) susceptibility artifact or susceptibility effect. The relaxation rate due to the static component of magnetic field inhomogeneities is denoted 1/T2′.

T2* represents the combination of T2 relaxation time and T2′ relaxation time, due to field inhomogeneities, and can be expressed as

$$1/T2* = 1/T2 + 1/T2' \qquad\qquad (1.5)$$

assuming that T2′ decay is exponential. The transverse relaxation attenuates exponentially after the radio frequency (RF) excitation and is defined as the free induction decay (FID). The relaxation time constants (T2, T2* and T2′) can be expressed as relaxation rates defined by R2 =1/T2, R2* =1/T2* and R2′ =1/T2′.

The MR signals generated above can be localized and encoded using magnetic field gradients that vary linearly with position inside the magnet and cause variation in **ω₀** as a function of position. Gradient coils generating these linearly varying magnetic fields are located within the bore of the primary magnet [39]. Three steps are used to produce two-dimensional (2D) MR images by applying a combination of RF and gradient magnetic fields; slice selection, spatial encoding, and frequency encoding. To excite protons within the desired slice, a one-dimensional slice-selection gradient and RF pulse are applied

simultaneously. This gradient field causes a linear change of resonance frequencies as a function of position. The RF pulse frequency matches the frequency included in the selected slice. The direction of the selected gradient determines the orientation of the slice. Instead of a single frequency, the excitation RF pulse is composed of a range of frequencies, identified as the RF transmit bandwidth. RF bandwidth and the strength of the gradient determine the slice thickness.

Spatial encoding within the slice can be achieved by using two techniques, frequency encoding and phase encoding, applied in an orthogonal direction with respect to each other. In frequency encoding, the magnetic field gradient is applied throughout signal acquisition. The location of the spins along the direction of the gradient can be recognized by the frequency of their emitted signals. In traditional 2D MRI, frequency encoding is not adequate by itself because it gives positional information only in one direction. Therefore, a phase encoding gradient field is applied as a short pulse before data acquisition, providing a phase distribution among the spins. To obtain position information from the phase, the process is repeated several times with phase encoding gradients of incrementally different amplitudes. The output data are recorded as a set of lines in a 2D signal array within a domain identified as K-space. Applying 2D Fourier transform to K-space data recovers the spatial distribution of the signal, an operation known as image reconstruction [40].

In general, the gradient echo sequence (GRE) is a manipulation of the FID signal. It starts by applying an RF pulse and slice-selective gradient (Gz) simultaneously. Shortly after that, a gradient (Gy) is applied in the phase encoding direction, followed by an external dephasing gradient field (Gx) across the tissue. These gradients cause a variation in local magnetic fields and consequently changes the resonance frequencies across the specimen. Dephasing of the FID is accelerated. Then the process is reversed, and a second gradient magnetic field is applied with opposite polarity to the dephasing gradient. The spins begin to re-phase until they are again in phase and a signal is generated. This single echo gradient echo sequence is shown in Fig 1.4. The same process can be repeated to produce multiple GREs after a single RF-pulse (see Fig 1.5. for a cardiac multiple GRE sequence.).
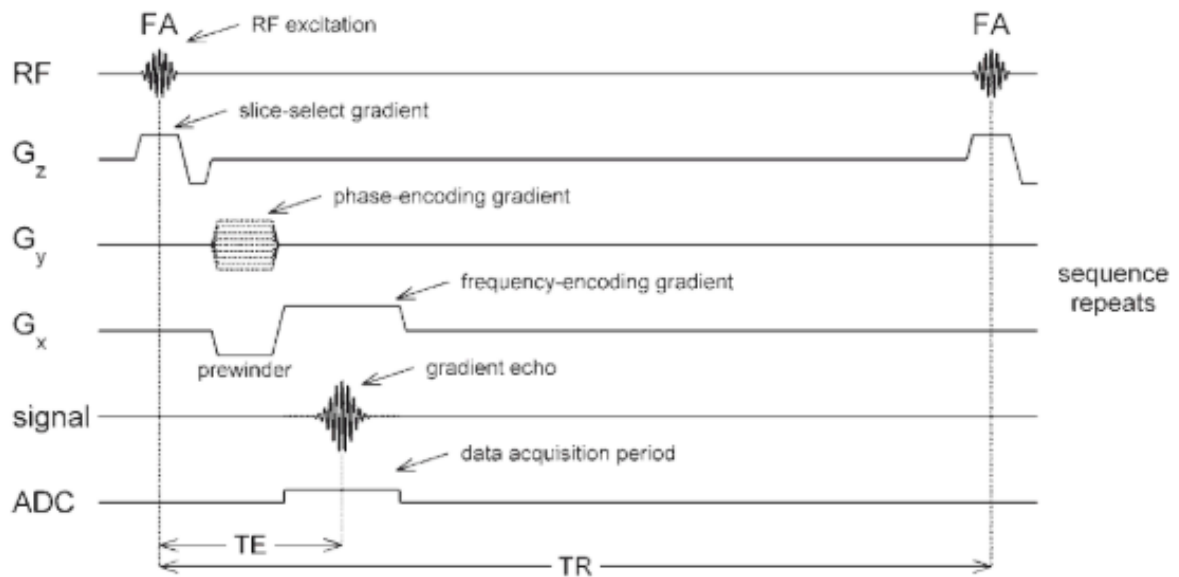
Figure 1. 4. Gradient echo image pulse sequence diagram. A simple pulse sequence implements slice-selection and within slice spatial encoding. The top line depicts the RF pulses, which rotates the magnetization toward the xy plane. The lines listed as Gz, Gy, and Gx designate the magnetic field gradient in slice-select, phase-encoding, and frequency-encoding directions, respectively. The analog to digital converter (ADC) is applied during signal acquisition [41].

1.3.2   Myocardial Hemorrhage Imaging

At the early stages of myocardial hemorrhage, it is difficult to visualize small quantities of red blood cells. Nevertheless, the specificity of MRI for detecting hemorrhage has been validated in vivo [42, 43].

Histopathological analysis has verified the potential of MRI sequences (based on T1-, T2- and T2*-weighted images) to diagnose myocardial hemorrhage [44, 45]. In particular, T2*-weighted imaging is currently the standard clinical method for diagnosing myocardial hemorrhage [34, 45]. Along with degradation of red blood cells, hemoglobin is broken down into several products (oxyhemoglobin, deoxyhemoglobin, methemoglobin, and hemosiderin) which influence MRI signal intensities. These vary based on electronic configuration of various hemoglobin by-products, with number of unpaired electrons (N) having the greatest influence on the MR signal [46, 47]. Deoxyhemoglobin and methemoglobin are best detected by T2- and T1-weighted sequences, respectively [48]. In addition, since lysis of red blood cells also releases ferritin and hemosiderin, iron deposition from multiple sources can be detected by T2- or T2*-weighted imaging [49]. While the observation of myocardial hemorrhage has prognostic value beyond that provided by the observation of microvascular obstruction alone, the relationship between myocardial hemorrhage and microvascular obstruction remains unclear. In addition, the effect of myocardial edema may limit the delineation of hemorrhage and, in the case of severe edema, hemorrhagic regions may be enormously underestimated [49, 50].

Despite these complications, CMR imaging using T2 and T2* shortening has improved the assessment of myocardial hemorrhage, owing to the elevated tissue density of paramagnetic hemoglobin breakdown products. Early studies by Lotan *et al.* [51, 52] illustrated T2* shortening concurrent with hemorrhage at 24 and 72 hours post-reperfusion in canine MI.

T2* mapping has subsequently been used in several patient and animal studies on myocardial infarction. These studies indicate that T2* mapping provides greater accuracy than T2 mapping in differentiating between hemorrhagic myocardium and healthy regions remote from the injury, and reduces the effect of myocardial edema [53]. We also note that

several studies have described a linear increase in rate of signal decay (R2* = 1/T2*) with hepatic iron level [54–60]. (This linear relation of R2* with iron is one reason that an R2* map may be more convenient than a T2* map.) Similar variations in R2* have been qualitatively correlated with cardiac iron deposition [61]. Myocardial hemorrhage is marked as a region of reduced signal intensity, in animal MI models and humans within the infarcted area on R2* maps, with R2* > 0.05 ms^{-1} [38, 53, 62, 63]. This threshold value for R2* was initially determined at 1.5 T but has been validated at 3 T. Some researchers have even suggested that the difference between R2 and R2*, called R2′, may be a more precise marker of tissue iron [64]. In a canine model of myocardial hemorrhage [65], the sensitivity and specificity of T2 imaging were found to be 98% (94–100%) and 90% (83–98%), for detection of the myocardial hemorrhage, respectively. For T2* the sensitivity and specificity were 95% (86–100%) and 94% (88–100%), respectively.

1.3.3 Cardiac multi-echo GRE sequence for T2* measurement

Here we briefly describe the CMR sequence used in this thesis for T2* mapping (Siemens WIP #44B.1, VB20P). With this sequence, the MRI signals are collected over multiple heartbeats. To achieve synchronization between the pulse sequence and signal acquisition during the cardiac cycle, ECG triggering is used. Also, the respiratory motion must be considered because it causes image degradation. This can be reduced using several approaches, such as acquisition during a breath hold and respiratory gating. Breath-hold was applied in the images analyzed for this thesis.

Figure 1.5 demonstrates the acquisition process starting after each ECG wave. Data are obtained through the T2* decay. Triggering is applied to acquire relatively static images at a certain time in the cardiac cycle. Typically, signals required to reconstruct a single T2* map are obtained at the same heart phase (in diastole) over multiple heartbeats.
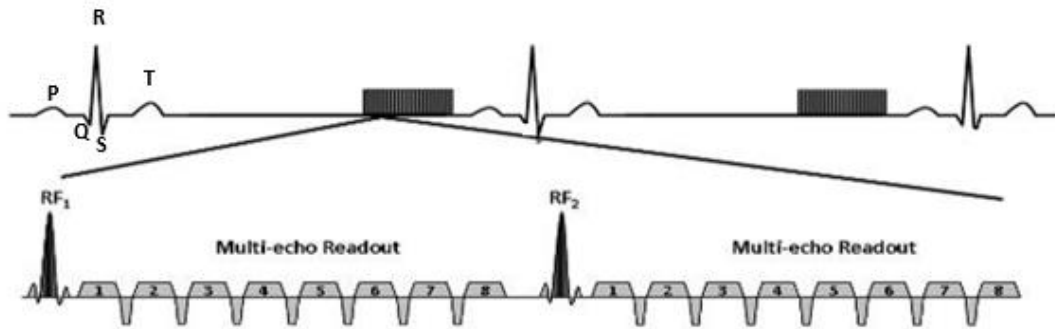
Figure 1. 5. ECG-triggered GRE sequence schematic. Signals are obtained following a predefined delay after the ECGR-wave. In the present work, eight echoes were collected in every repetition time (TR) to produce eight T2*-weighted (T2*W) images. Nine to ten k-space lines were obtained in each cardiac cycle. Echo times ranged from 3 to 23 ms. This figure is reproduced with permission from Siemens Health Care and Sven Zuehlsdorff (Siemens Health Care).

For so-called black blood images, the blood pool signal is suppressed using two additional 180° RF inversion pulses. The first pulse inverts the magnetization of the entire volume of blood and tissue within the RF coil (i.e., nonselective). The second inversion pulse returns the magnetization of the desired slice to be imaged. The resultant effect of these two pulses is to return the magnetization within the slice to its state before applying the first RF excitation pulse and to invert the magnetization of tissue and blood outside the slice. The blood streaming into the slice will have a dark signal, since blood has left the slice by the time the second inversion pulse is applied. Thus, the acquired images provide a distinct boundary between chamber and myocardium

1.4   17-Segmentation LV model: the polar plot map

In 2002, The American Heart Association (AHA) introduced a 17-segment model, providing regional analysis of the LV [66]. This 17-segment model is applied for imaging slices in the short axis orentation. To consider anatomical variations in the LV that result from patient to patient variability, several cardiac imaging modalities have been used to achieve a consensus for regional analysis of the LV, including computed tomography (CT), coronary angiography, positron emission tomography (PET), single-photon emission computed tomography (SPECT), and MRI [67, 68]. In this bulls-eye map, quantitative data generated from these imaging modalities have been used to create a polar plot based on the standard 17-segment model [69, 70]. These polar plots from tomographic images of the LV have been employed for regional analysis of cardiac function, like wall thickening or myocardial perfusion.

The plots consist of three concentric rings, stacked together as shown in Figure 1.6 A. Each ring represents a short-axis view through the LV. The first (outer) ring corresponds to the basal region of the heart, the second ring represents the mid-cavity, and the third (and smallest) ring is at the apex of the heart. The center of the polar plot outlines the apical cap where the cavity ends. Both basal and mid-cavity rings are arranged into six portions numbered 1−6 and 7−12, respectively. The numbers start anteriorly and continue counterclockwise around the ring. The apical ring is partitioned into only four segments numbered 13−16 due to its smaller size. The apical cap is indicated by one segment (17 in Figure 1.6A). The distribution of myocardial mass within the basal, mid-cavity, and apical segments is 35%, 35%, and 30%, respectively. Different myocardial segments have been assigned to the main coronary arteries (RCA, LAD, and LCX in Figure 1.6 B).

(A)
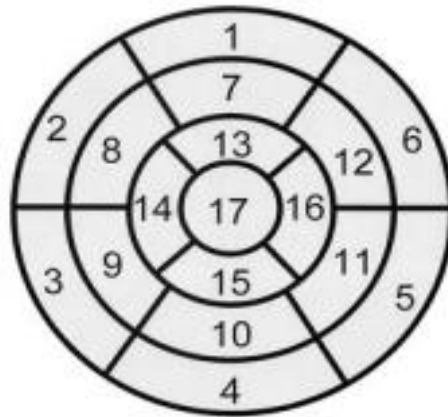
1. basal anterior	7. mid anterior	13. apical anterior
2. basal anteroseptal	8. mid anteroseptal	14. apical septal
3. basal inferoseptal	9. mid inferoseptal	15. apical inferior
4. basal inferior	10. mid inferior	16. apical lateral
5. basal inferolateral	11. mid inferolateral	17. apex
6. basal anterolateral	12. mid anterolateral	

(B)
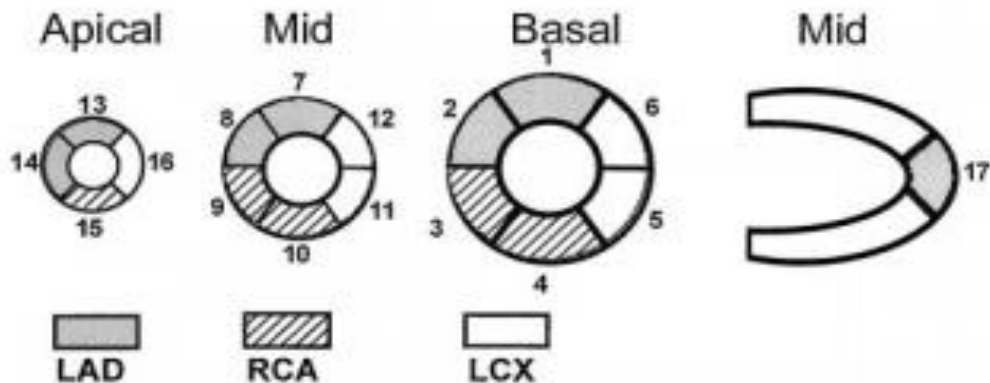
Figure 1. 6. Drawing of the 17-segment LV model. (A) The 17 segments of the polar plot are shown, with the nomenclature identifying anatomical regions of the tomographic image. Numbered segments begin at the base of the LV and progress toward the apex. (B) While the main coronary arteries supply different regions of the LV, each ring is affected by all three of the major arteries. The LAD generally serves the apex (17) and anteroseptal regions (1-2, 7-8 and 13-14); the RCA generally serves the inferoseptal regions (3-4, 9-10 and 15); and the LCX generally serves the lateral regions (5-6, 11-12 and 16) [71].

1.5   Graphical Techniques: The Probability Plot

Many graphical methods such as a histogram or a stem plot can be used to reveal non-normal features of a distribution, for example, outliers, skewness, and clusters [72]. These features provide an indication of the appropriate distribution model for the data. The probability plot is a graphical method for assessing whether or not data exhibit a standard normal distribution (i.e. a Gaussian distribution). For a given distribution of (n) data points, the data can be ordered from smallest, which is called the first order statistic to the largest. The probability (percentile) value which is defined as the order statistic medians for the given distribution (Ui) is described by [73]:

$$U_i = 1 - U_n \quad \text{for } i = 1 \tag{1.6}$$

$$U_i = (i - 0.3175)/(n + 0.365) \quad \text{for } i = 2, 3, ..., n\text{-}1 , \tag{1.7}$$

$$U_i = 0.5^{(1/n)} \quad \text{for } i = n \qquad . \tag{1.8}$$

For a given data distribution, the probability plot is created by plotting the actual data against the probability (percentile) that individual value occupies. The pair points (actual data, probability) can be fitted to a line that is designated as a reference line, which represents a theoretical normal distribution. Deviation from the straight reference line indicates deviation from normality [74] (Figure 1.7).
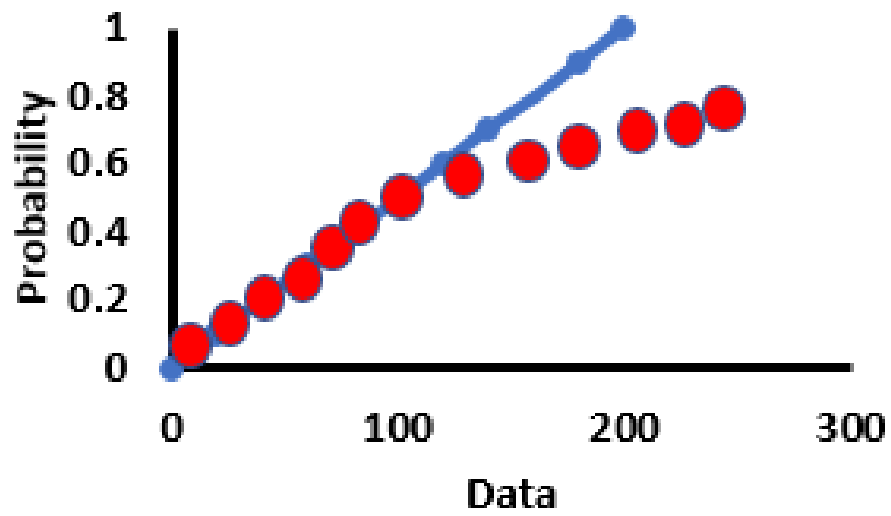
Figure 1. 7. Probability plot test for random data. The graph shows theoretical data to illustrate where the points deviate from the theoretical straight line (blue) and follow a non-Gaussian distribution.

1.6   Overview of the thesis

CMR has achieved clinical importance in the noninvasive evaluation of myocardial viability and function post-MI, allowing for high-resolution assessment of AAR, infarct size, and MVO. These in turn are strong predictors of myocardial hemorrhage which often happens following MI [75]. Hemorrhage indicates the extravasation and accumulation of red blood cells in cardiac tissue and is a demonstration of acute microvascular injury [43, 76, 77] . The MI also leads to inflammation and this too influences the healing process [78]. Responses post-MI also affect the detection of myocardial hemorrhage. For example, the region of MVO may considerably overlap with the area of hemorrhage [43] and in the presence of edema, the hemorrhagic zone may be greatly minimized [3].

Despite these confounders, the specificity of MRI for detecting hemorrhage has been validated in several experimental studies [79–81]. Visualization of hemorrhage is attributed to the degradation of erythrocytes, which leads to iron deposition that can be detected on T2*-weighted MR images [3, 45]. In one of the currently accepted approaches for differentiating between hemorrhagic and remote tissue, manual delineation of the remote tissue is based on the late gadolinium-enhanced MR images of the region that manifests no hyperintensity. This region is used as a reference on T2*-weighted images. Hemorrhagic regions are identified on T2*-weighted images with mean signal intensity of at least 2 standard deviations (SD) below the reference region [82]. Developing an automated segmentation of the hemorrhagic region would be valuable for analyzing the temporal evolution of myocardial hemorrhage, and/or other iron-related changes (e.g. due to monocyte infiltration post-MI).

In the present work, we propose an automated segmentation method based on a stabilized probability plot, which is a graphical method for assessing whether or not a data set is approximately normally distributed [74]. We applied this method to examine the distribution of the relaxation rate values in the LV for baseline (non-infarcted) cardiac tissue to determine a threshold below which R2* values follow a normal distribution. We demonstrate that this method shows potential for future work (perhaps with more advanced analysis and shimming) but could not be applied to the post-MI images in the present work. Instead we chose a global threshold based on the highest R2* values in baseline images

and applied that threshold to segment post-MI images into remote tissue (below threshold) and tissue that may be abnormal (above threshold). This baseline study also provides insight into the extent and distribution of R2* in the canine LV and illustrates substantial regions of high R2* which may be associated with macroscopic magnetic field variations (sometimes referred to as susceptibility artifacts).

In the model of canine MI that was used in the images that we (retrospectively) analyzed, occlusion of the LAD artery typically causes an MI in the LV. While multiple regions of the LV may be affected, this type of MI rarely affects the inferior side [83–85]. To provide spatial orientation in the context of our analysis, we used polar plots to represent the LV based on the 17-segment model developed by the AHA. Also, using a threshold R2* value from baseline images, we investigated the change in R2* and volume of "abnormal" tissue as a function of time (number of days) post-MI.

The following three objectives outline the main experimental goals of this study.

The first objective was to determine the region with relatively low and uniform R2* values by examining the distribution of R2* values within baseline R2* maps of the entire LV. To address high R2* values in the LV, we used an automated thresholding algorithm, based on an iterative selection method, to identify regions with relatively uniform R2* values within baseline R2* maps (i.e. little or no artifacts due to motion, susceptibility). We investigated the extent to which the R2* values in this region followed a normal distribution. In addition, we compared the mean R2* value of this uniform region with the value reported in literature: 0.03-0.050 ms^{-1} [2, 86, 87].

The second objective was to use the selected region (identified in the first objective) in baseline image analysis. For R2* values in this region, we chose a threshold value very close to the highest value in the baseline polar plots. This provided a reference point below which we considered the post-MI myocardium as healthy.

The third objective was to apply the new threshold (objective 2) in the LV post-MI and thereby examine changes in R2* associated with changes in tissue iron. With this analysis, we studied the changes in R2* and volume of "abnormal" tissue as a function of time post-MI. We also studied these changes based on a previously published [88]

threshold ($R2^* > 0.05$ ms^{-1}) and compared the resulting time evolutions from these two thresholds.

Chapter 2: Methods

2　Background

The primary cause of MI is a build-up of atherosclerotic plaque in the coronary artery (Figure 1.2). A rupture in the plaque forms a thrombus which in turn reduces the flow of blood to the muscle, causing ischemia. This creates either a partial or complete decrease in oxygen to the muscle depending on that vascular supply, and also necrosis, which is death of myocardial cells or tissue [12].

Severe microvascular injury with or without reperfusion may result in myocardial hemorrhage or iron deposition, respectively, and both are associated with left ventricular systolic dysfunction [25], a form of adverse remodeling associated with changes in heart size and function [26, 27], and poor clinical outcomes [28].

Cardiovascular magnetic resonance (CMR) imaging has achieved clinical importance in the noninvasive evaluation of myocardial viability and function post-MI, allowing for high resolution depiction of the infarct size. Visualization of hemorrhage is attributed to the degradation of erythrocytes, which leads to iron deposition that can be detected on T2*-weighted MR images [3, 45]. Along with degradation of red blood cells, hemoglobin is broken down into several products (oxyhemoglobin, deoxyhemoglobin, methemoglobin, and hemosiderin) which influence MRI signal intensities. The breakdown products of hemoglobin are paramagnetic and hence lead to shortening of T2* relaxation times. A hypointense core within the infarcted myocardium in T2-and T2*-weighted CMR has been correlated with hemorrhagic infarcts [37, 38]. However, a reliable assessment of myocardial hemorrhage in T2*-weighted images of the entire LV is challenging due to image artifacts, the presence of edema, and manual delineation of the hypointense zone, which is prone to observer error.

Studies have indicated that T2* mapping provides greater accuracy than T2 mapping in differentiating between hemorrhagic myocardium and healthy regions remote from the injury, and reduces the influence of myocardial edema [53]. Whether examining cells or tissue, there is a linear increase in the rate of signal decay ($R2* = 1/T2*$) as a function of iron content [54, 89]. Variations in R2* have also been qualitatively correlated with cardiac

iron deposition [2]. In an accepted clinical approach, myocardial hemorrhage is marked as a region of reduced signal intensity within the infarcted area on R2* maps, where R2* > 0.05 ms^{-1} [38, 53, 62]. However, identifying an appropriate R2* value for healthy myocardium would be valuable for analyzing the temporal evolution of myocardial hemorrhage, and/or other iron-related changes (e.g. due to monocyte infiltration) post-MI. For this purpose, we examined myocardial T2* at 3 T in a canine MI model using T2* mapping.

Many graphical methods such as a histogram or a stem plot can be used to reveal non-normal features of a distribution, for example, outliers, skewness, and clusters [72]. The probability plot is a graphical method for assessing whether or not data exhibit a standard normal distribution (i.e. a Gaussian distribution). For a given data distribution, the probability plot is created by plotting the actual data against the probability (as a percentile) that individual value occupies. The pair points (data, probability) can be fitted to a line that is designated as a reference line. If the data is normally distributed, the normal probability plot will follow the reference line. Deviation from the straight reference line indicates deviation from normality [74]. The point at which R2* (the data) deviates from normality provides a threshold above which voxel by voxel analysis of elevated R2* may be spatially identified.

In our analysis, we recorded spatial information using the AHA recommended polar plot of the LV [65]. Assembled from tomographic images of the LV, the bull's eye map has been employed for regional analysis of cardiac functions, like wall thickening or myocardial perfusion. Moreover, different myocardial segments in the polar plot have been assigned to the main coronary arteries (Figure 1.6B), facilitating a comprehensive assessment of the cardiac injury.

The study in this thesis involves a retrospective analysis of canine CMR images as well as CMR images from two healthy human adults. The canine data includes images acquired following experimentally induced myocardial infarction (permanent occlusion) as well as baseline images (i.e., images acquired prior to MI). The animal data had been acquired as part of another study and the experimental procedure for inducing MI is described elsewhere [90]. The human images were acquired in order to test how changes to the

acquisition might influence susceptibility related artifacts. Unless otherwise noted, all GRE images were processed using MATLAB 7 R2010b (Mathworks, Nattick, MA, USA)

2.1 Methods

2.1.1 CMR acquisition of baseline images

The baseline CMR images that were retrospectively analyzed for this thesis had been obtained from six adult female canines studied according to protocols approved by the Canadian Council on Animal Care. CMR images were obtained with a Siemens Biograph mMR 3 T scanner. Short axis views (10 slices) covering the entire LV utilized a CMR multi-echo (8 echoes) GRE T2* sequence (Siemens Work-in-Progress; WIP #44B.1, VB20P, Figure 1.5) and were performed with both bright and dark blood imaging techniques. Each slice was acquired in one breath-hold. Typical acquisition parameters were: bandwidth 925 Hz/pixel; flip angle: 10° for 5 of the canines and 20 ° for one canine; matrix size 208x102; spatial resolution 1.4 x 1.4 x 12 mm^3; TE: 2-13 ms; slice thickness 6 mm.

2.1.2 CMR acquisition of post-MI images

The post-MI images that were retrospectively analyzed for this thesis involved four adult female canines studied according to the protocols approved by the Animal Care Committee of Western University (Protocol 2011-67). Propofol was used to induce anesthesia and controlled with (2%) isoflurane. An MI was produced by putting a snare ligature around the LAD for the duration of the study. Animals with this permanent occlusion were imaged at 3, 8, 15, 21, and 41 days post-MI. In each animal, CMR images were acquired at 3 T in 10-13 contiguous short-axis slices covering the entire LV. A multi-echo (8 echoes) GRE T2* sequence was performed with a dark blood imaging technique. Typical imaging parameters utilized to acquire images were: bandwidth 814 Hz/pixel; flip angle: 20°; FOV:

217x290 mm^2; matrix size 256x192; spatial resolution 1.4 x 1.3 x 12 mm^3; TR: 441 ms; TE: 3-23 ms; slice thickness 6 mm.

2.1.3   CMR acquisition of healthy volunteers

The goal of involving healthy human adults was to investigate the influence of slice thickness on R2* measurements. This study was performed in accordance with a University of Western Ontario Health Studies Research Ethics Protocol (Protocol 2011-67). Two Volunteers were invited to participate in this study. For each volunteer, informed consent was obtained prior to the study.

CMR images were obtained on a Biograph mMR 3 T scanner (Siemens, Erlangen, Germany). Images were collected during breath hold and with ECG synchronization. Images were acquired in 3 short-axis slices (apical, mid and basal), utilizing a multi-echo (8 echoes) GRE T2* sequence performed using dark and bright blood imaging techniques. Typical acquisition parameters were: bandwidth 930 Hz/pixel; flip angle: 10 °, 20 °, and 30 °; FOV: 340x340 mm^2; matrix size 256x256; spatial resolution 1.4 x 1.3 x 12 mm^3; TR: 200 ms; TE: 2-13 ms; slice thicknesses 4 and 6 mm. (The minimum slice thickness permitted with this sequence was 4 mm.)

2.1.4   Myocardial R2* calculation and R2* map construction

LV contours, including endocardial and epicardial borders were manually drawn using the image with the shortest echo time in each slice. The delineation of myocardium was made with enough consideration to the separation from tissue intersections to minimize the partial volume effect, especially between myocardium and blood. The segmented myocardium was represented as a binary image (mask) with ones (1) representing the LV myocardium and not a number (NaN) representing elsewhere. The area of the LV

myocardium was confirmed on CMR short-axis images by pixel multiplication with the corresponding pixel masks.

Noise on MR signals manifests itself as a Rician distribution in magnitude images [91]. MR signal amplitude is affected by the distribution of Rician noise. When SNR is low, the signal must be corrected prior to R2* fitting to compensate for the Rician distribution of noise. The corrected MR signal (S) of T2* decay can be evaluated by [92]:

$$S = \sqrt{S_{un}^2 - 2\sigma^2} \quad , \qquad (1.9)$$

where S_{un} is the magnitude signal value for a given pixel at a given time and σ is the mean signal value over a background region of the T2*-weighted images. For this thesis the procedure for measuring background involved selecting a 20×20 pixel square in the corner of an image (i.e. an area with no CMR signal). The decay curve obtained was fitted to a mono-exponential curve

$$S(t) = S(0)e^{(R2^*)(TE)} \qquad (2.0))$$

Images of the segmented myocardium were processed to generate *R2* (1/T2*)* maps by applying mono-exponential curve fitting to the signal on a pixel by pixel basis.

2.1.5   R2* Precision and Goodness of Fit

The goodness of fit was evaluated utilizing the coefficient of non-determination $(1 - r^2)$ defined by

$$1 - r^2 = \frac{SE_{model}}{SE_{\bar{y}}} \qquad (2.1)$$

where r is the correlation coefficient, $SE_{model} = \Sigma(y_i - \hat{y})^2$ is the total squared error between the experimental data (y_i) and the predicted value based on the regression model $(\hat{y})$. $SE_{\bar{y}} = \Sigma(y_i - \bar{y})^2$ is the total squared error between (y_i) and the mean of the (y_i)

28

values, and $1 - r^2$ represents the total variation in the actual data that is not described by the model.

The uncertainty in R2* values was obtained from the 95% confidence intervals provided by the Matlab fit function. In particular, we divided this confidence interval by 4 to produce a standard error (STE), i.e., ½ of the 68% confidence interval.

Previously it was suggested that the later echoes should be eliminated from T2* fitting as background noise, motion and susceptibility image artifacts in these echoes may affect the MRI signals and degrade the R2* analysis [93]. Therefore, we examined the impact of number of echoes used in the R2* fitting procedure on uncertainty and goodness of fit. For baseline short axis images, STE and $1 - r^2$ maps were generated for the entire LV with 8, 6 and 5 echoes.

2.1.6   Fitting MRI signal to region of interest

In addition to the voxel-by-voxel fitting, the mono-exponential model was applied to a region of interest (ROI). In baseline images, an ROI covering the interventricular septum was chosen to avoid susceptibility artifacts. In post-MI images, an ROI occupying the non-normal (potentially injured tissue) R2* region was chosen to illustrate shortening of the MR signal.

2.1.7   Bulls-eye map construction

An R2* map was generated for each slice of the entire LV (starting at the most apical slice and moving to the most basal slice). For each R2* map, a 4- degree sector rotated around the entire slice permitted a radial sampling of the map (Figure 2.1). The center of rotation was defined as the center of the LV. The mean value of R2* was determined for each of the 90 segments of the myocardium within each slice. This gave 90 R2* values ($4^{\circ} \times 90 = 360^{\circ}$). The process was repeated for all slices of the entire LV (ending with the basal slice). These data were arranged into matrix form, with each row of the matrix consisting of R2* values for each sector around the circumference of a given slice. The final matrix formed

has the dimension of 90 × number of slices. A Matlab function was used to fill the standardized 17-segment model of the LV with the matrix values (Figure 1.6).
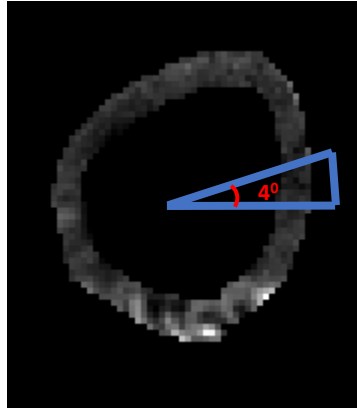
Figure 2. 1. Radial sampling of the myocardial R2* map. A 4- degree sector (outlined in blue) was used to sample the R2* map of a single slice. The sector was rotated counter-clockwise over the R2* map. Background values were set to equal zero and excluded from calculations.

Six polar plots were generated, one for each animal for which baseline data was available. These polar plots were then averaged to generate one composite polar plot. To identify the uniform region of the composite polar plot with relatively low susceptibility artifact, an automated thresholding algorithm, based on an iterative selection method [94] was used. In this method, the half maximum dynamic range was used as an initial threshold to segment the histogram into two regions. The mean of the samples associated with pixels from these two regions were then computed. The average of the two means sampled is considered as the new threshold. Based on this new value, the computational process is reiterated until the threshold does not change. This segmented area was tested using the probability plot to identify the distribution of lower mean R2* values. This area was designated as the uniform baseline region and was used to analyze polar plots of post-MI images.

In this region, the change in the R2* values from each baseline polar plot, is determined by the coefficient of variation (CV) as:

$$CV = \frac{SD}{M}$$
(2.2)

where SD and M are the standard deviation and the mean value of the R2* measurements, respectively.

2.1.8   Probability Plot Method

The probability plot is a graphical method to distinguish a deviation from normality. The normal probability plot confirms that a hypothesis of normality is reasonable. The data (i.e. R2* values) are arranged in ascending order and the normal probability plot is constructed by graphing data versus normal order statistic medians (using the equations described in section 1.5). The points are fitted to a reference line that represents a theoretical normal distribution: the points departing from this line indicate deviations from normality. The point at which data start to depart from the straight reference line represents a threshold that distinguishes between Gaussian and non-Gaussian distribution (Figure 2.2). Mathematical calculations were performed using the Matlab function: probplot ('normal',data). This method can also show the nature of the departure from normality (e.g., skewed data have a short or long tail).
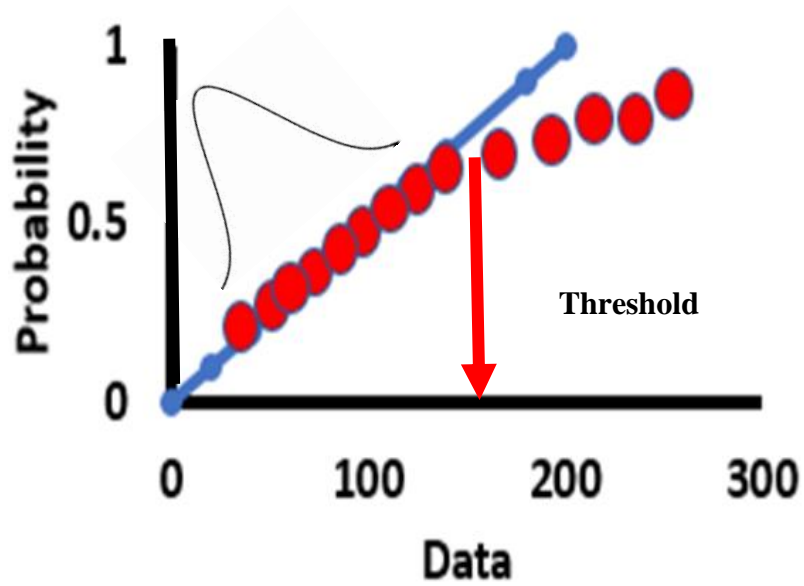
Figure 2. 2. Threshold determination technique. Data were tested using the probability plot method. Threshold (red arrow) is the point where data deviates from a Gaussian distribution, shown by the theoretical straight line (in blue), and provides a value above which data deviate from normality.

2.1.9   Analysis of R2* images

For baseline polar plots, only the uniform baseline region was considered in the composite baseline polar plot, as explained in section 2.1.7. The stabilized probability plot method was applied to this area to examine the distribution of R2* values within this uniform baseline region. We determined the critical point (visually) where the distribution of R2* values change from a normal to non-normal distribution.

The motivation for using the probability plot method on baseline images was to determine if it could be used for post-MI differentiation of abnormal versus normal tissue. However, our results showed that while the method has potential for future application, on these baseline images it led to the selection of relatively large regions as being "abnormal". Hence we chose not to utilize this method for post-MI analysis. Instead, we determined a general threshold as follows. For each of the six polar plots, we determined the 95th percentile of R2* values. The highest of these six values was used as a threshold for post-MI analysis.

For post-MI images, the threshold value was applied within the region that was found to be uniform on baseline images. The rationale for this was that we assumed that this region of the LV would have minimal susceptibility-related contributions to R2*. In the post-MI polar plots, the threshold was applied to segment the LV into high R2* region (considered as "abnormal") and low R2* region (normal). The mean R2* values of abnormal R2* regions were calculated over time post-MI. We also determined the volume of tissue, relative to the volume of the uniform baseline region, with R2* values above the proposed threshold. This measure will be referred to as the percentage of ROI volume with high R2* (%LV). The results were compared with the common threshold ($R2* > 0.05$ ms^{-1}) [34].

2.1.10   Statistical analysis

To examine possible alterations in the mean R2* values over five-time points post-MI, we compared the values using repeated measure ANOVA at $\alpha = 0.05$ (IBM SPSS Statistics, version 25) for each of the three conditions ($R2* > 0.05$ ms^{-1}, $R2* > 0.08$ ms^{-1}, and $R2* < 0.08$ ms^{-1} (remote tissue)). To this end, we compared alterations in threshold values

within each threshold (0.05 ms^{-1} and 0.08 ms^{-1}) at time points of 3, 7, 15, 21 and 41 days post-MI. In addition we comapred threshold values of 0.05 ms^{-1} and 0.08 ms^{-1} at the same time points. Using a mixed model ANOVA, we compared %LV between two thresholds (0.08 ms^{-1} vs 0.05 ms^{-1}) at time points of 3, 7, 15, 21 and 41 days post-MI.

3   Results

3.1 The signal decay model

Figure 3.1 illustrates the mono-exponential decay model applied to a multi-gradient echo signal from a ROI covering the mid-ventricular septum of a representative baseline image. The mean R2* value in the interventricular septum for 3 slices (apical, middle and basal) was 0.050 ± 0.005 ms^{-1}. R2* values, based on ROI exponential fitting were measured in 3 dogs.
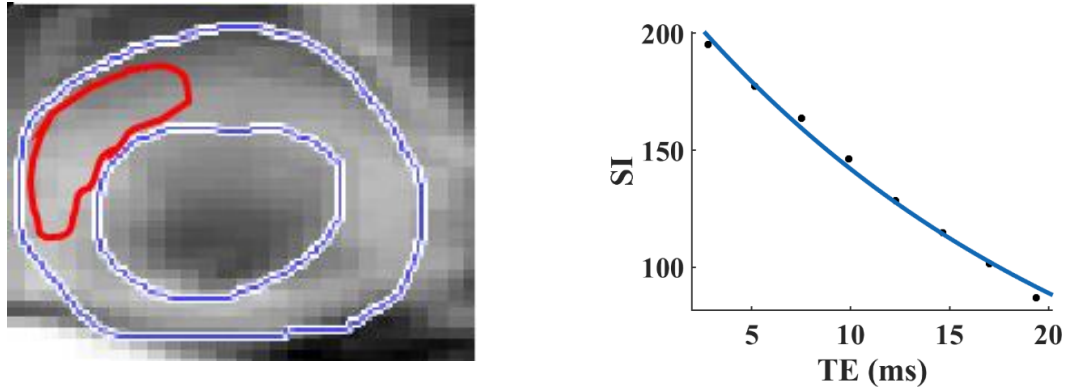
Figure 3. 1. A mono-exponential decay model. The left-hand panel shows a baseline T2*- weighted image of the LV with an ROI outlined in red within the mid-ventricular septum. The right-hand panel shows a plot of signal intensity at each TE acquired (2-19 ms). The mono-exponential curve was fitted to derive the R2* (1/T2*) value.

3.2 Effect of number of images on R2* measurements

Figure 3.2 illustrates representative baseline polar plots of R2*, STE and $1 - r^2$ obtained from one dog using either all 8 echoes or only with the first 5 or the first 6 echoes for the fitting procedure. Visual inspection of the polar plots shows that reducing the number of

echoes did not reduce the spatial variation of R2*. In addition, higher STE and $1 - r^2$ values were obtained with fewer echo numbers, indicating greater variability in R2* upon omission of data collected at later TE. Table 1 shows the mean values for R2*, STE and $1 - r^2$ over 3 subjects. These data suggest that all eight echoes should be used for further analysis. Additional results are in Appendix (A).
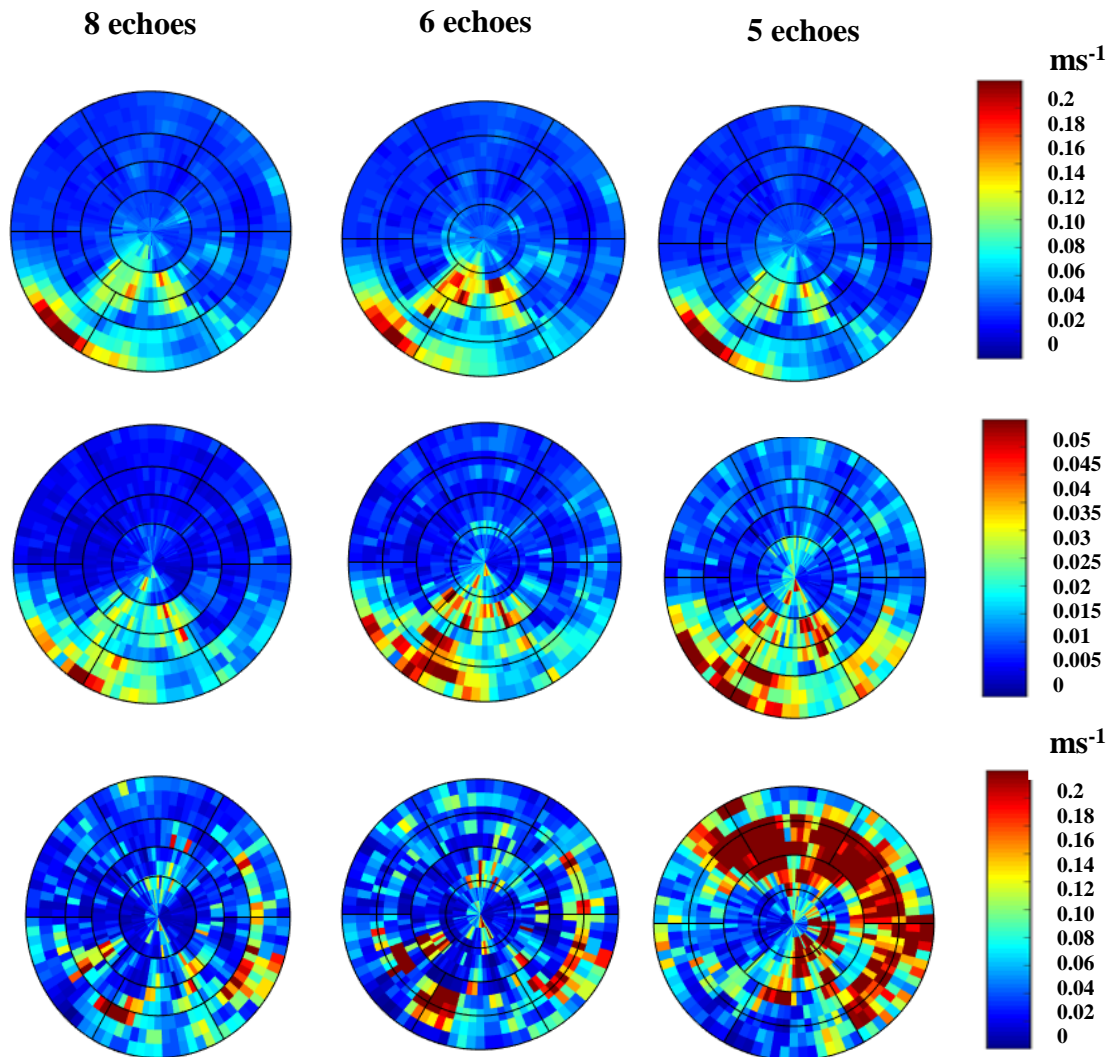
Figure 3. 2. The influence of number of echoes on R2*, STE, and $1 - r^2$ maps. The upper row shows R2* maps, the middle row shows STE maps and the lower row shows $1 - r^2$ maps, for baseline polar plots of the entire LV of one dog using, 8, 6 and 5 echoes. There was no significant variation in R2* polar plots with fewer echoes (upper row).

Higher STE (middle row) and $1 - r^2$ (lower row) values were obtained by excluding later echoes.

Table 1. Mean R2*, STE and $1 - r^2$ for the entire LV relative to the number of echoes / slice used for generating R2* maps.

Number of echoes	Mean R2* (ms^{-1})	Mean STE	Mean $1 - r^2$
8	0.046 ± 0.020	0.015	0.15
6	0.048 ± 0.025	0.020	0.20
5	0.044 ± 0.026	0.026	0.25

* Mean refers to the average over all sectors and over 3 dogs.

3.3 Healthy volunteer R2* measurements

Data from two male healthy volunteers (age range = 28 to 42) with no history of MI was acquired in order to determine if R2* would be reduced by reducing slice thickness, thereby suggesting that macroscopic magnetic field spatial variation contributes to R2*. A comparison between 6 mm and 4 mm thick slices at the levels of apex, middle and base of the LV with both bright and black blood imaging is shown in Table 2. This data shows larger mean R2* values with 6 mm vs. 4 mm slice thickness. By these findings, the black-blood sequence with thinner slice thickness improves R2* measurements.

Table 2. Mean R2* values for different slice thicknesses, standard deviation (SD) and difference in R2* between 6 mm and 4 mm slice thickness values.

		Bright Blood			Dark Blood		
		Slice thickness			Slice thickness		
	Volunteer	4 mm	6 mm	Difference	4 mm	6 mm	Difference
Apex	Volunteer1	0.030	0.047	0.017	0.040	0.047	0.007
	Volunteer2	0.040	0.045	0.005	0.041	0.045	0.004
Mid	Volunteer1	0.046	0.057	0.011	0.037	0.042	0.005
	Volunteer2	0.041	0.052	0.011	0.041	0.047	0.006
Base	Volunteer1	0.047	0.052	0.005	0.047	0.057	0.010
	Volunteer2	0.040	0.045	0.005	0.046	0.053	0.007
Mean +/- SD				0.010 ± 0.004			0.006 ± 0.002

 * Data obtained from 2 volunteers

3.4 Spatial variation of R2* at baseline

Polar plots of R2* maps at baseline demonstrate the variation in R2* values through the entire LV (Figure 3.3). We noted a substantial degree of heterogeneity in the inferior-septal region (segments 3, 4, 9, 10, 14, 15 and 17) of baseline plots, suggesting that macroscopic magnetic field variations may be large in these segments. Additional results are in appendix (B and C).
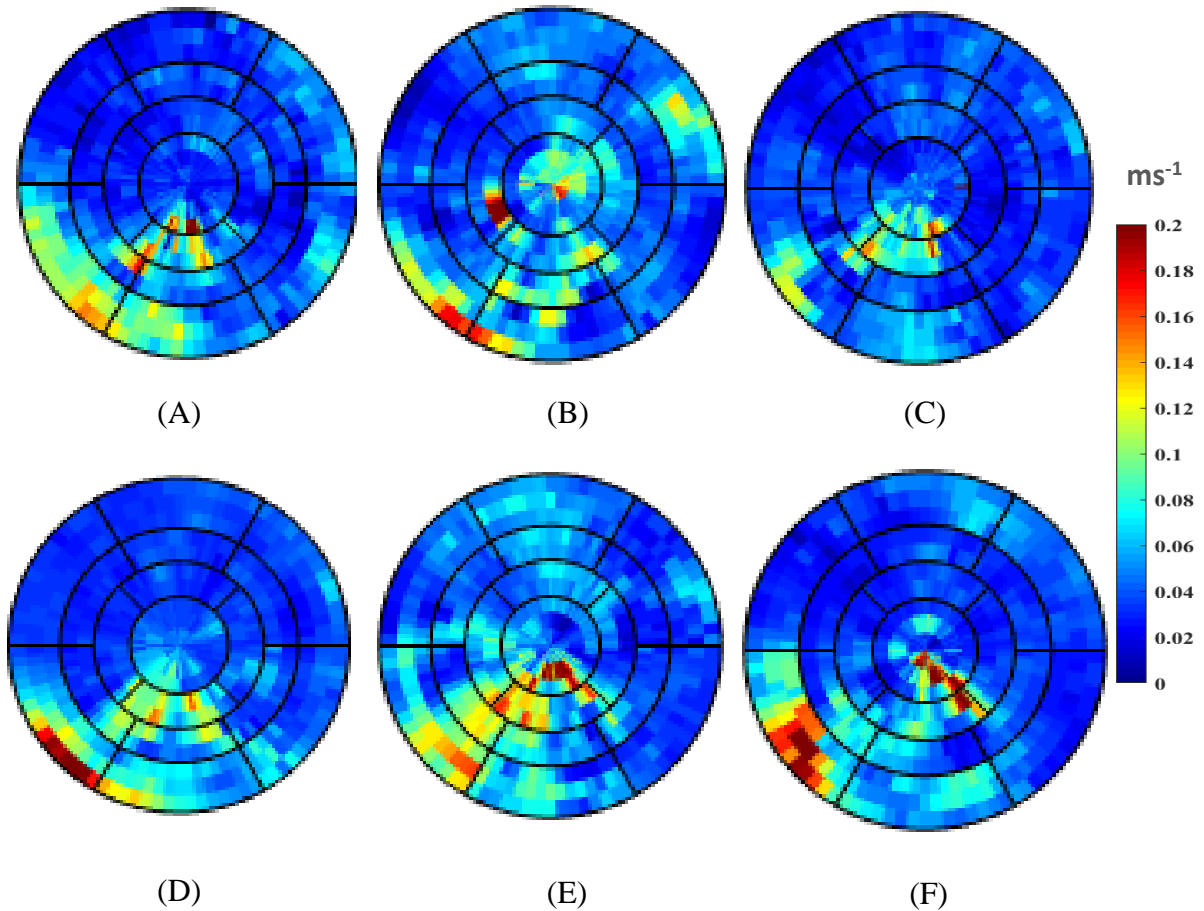
Figure 3. 3. Baseline R2* relaxation rates. Polar plots represent the 17 segments of the basal (outer ring), mid-ventricular (middle ring) and apical (central ring) short-axis planes of the LV from each canine subject (A-F). For these baseline R2* maps, data in A and B were generated with a bright blood sequence and flip angle of 10^0. Data in C-F were generated with a black blood sequence and flip angle of 10^0, with the exception of D, where flip angle was 20^0.

3.5 R2* segmental analysis at baseline

Polar plots from the six baseline images (Figure 3.3) were averaged, resulting in one composite R2* polar plot (Figure 3.4A). The mean R2* $\pm$ SD value in all subjects was 0.048 ± 0.015 ms^{-1}. Figure 3.4B illustrates the segmental analysis of the composite polar plot. The inferior-septal region represented by segments 3, 4, 9, 10, 14, 15 and 17 showed higher spatial variation compared to the remaining segments. This indicates that the inferior-septal zone is affected by artifacts (likely susceptibility-related) more than the lateral, anterior, and septal zones. The mean values of inferior-septal and unaffected zones are significantly different: 0.06 ± 0.01 ms^{-1} versus 0.041 ± 0.02, respectively, p<0.001.
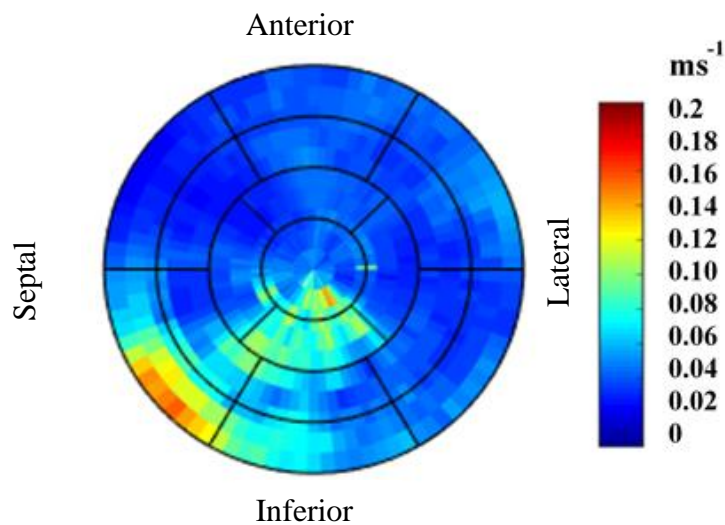

(A)
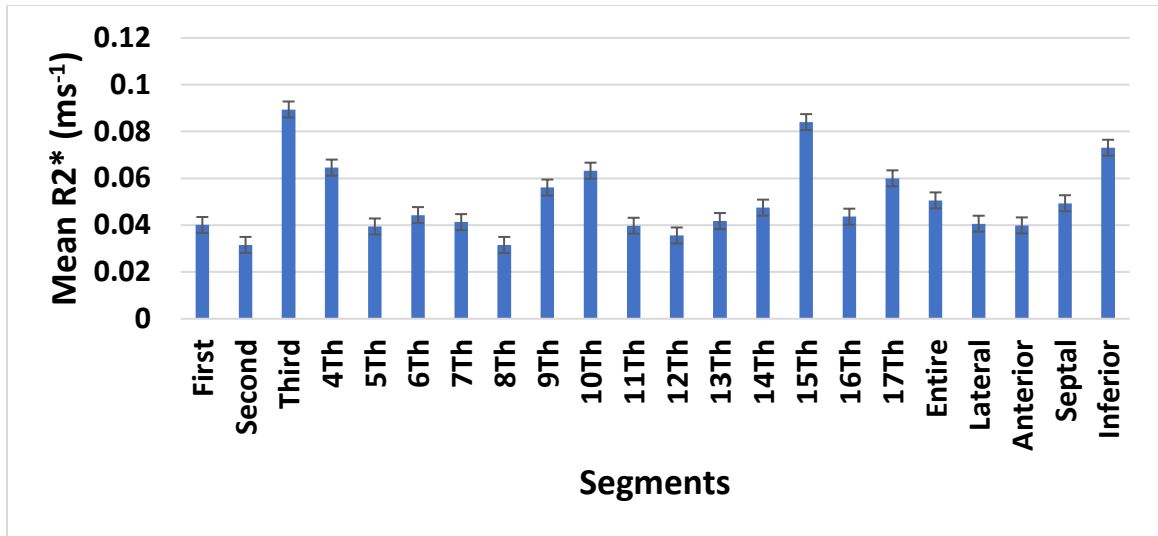
(B)

Figure 3. 4. Segmental analysis of the composite baseline polar plot for R2*. A) The polar plot shows the average polar plot over all animals (n = 6), providing a standardized baseline for the entire LV. B) Segmental analysis shows the variation in mean R2* values across the entire LV based on the 17-segmental model. The analysis indicates that the inferior septal region represented by segments 3, 4, 9, 10, 14, 15 and 17 has higher mean R2* values compared to the overall mean value (0.042 ± 0.007ms^{-1}) for the baseline myocardium. The vertical bar represents SD for mean R2* in each segment.

Figure 3.5A and B illustrate the region (in red) within the composite baseline R2* polar plot that is spatially relatively uniform, based on the application of an iterative selection algorithm (refer to section 2.1.7). This is taken to be a region with minimal susceptibility-related artifact due to macroscopic magnetic field variations. Figure 3.5B shows that the distribution of R2* values in the region outlined in red follows an approximately normal distribution based on the probability plot test. This region will be used for post-MI analysis (the uniform baseline region). Since the inferior-septal region has very high R2* values at baseline (possibly from susceptibility related contributions to R2*), it was excluded from the analysis of post-MI images.
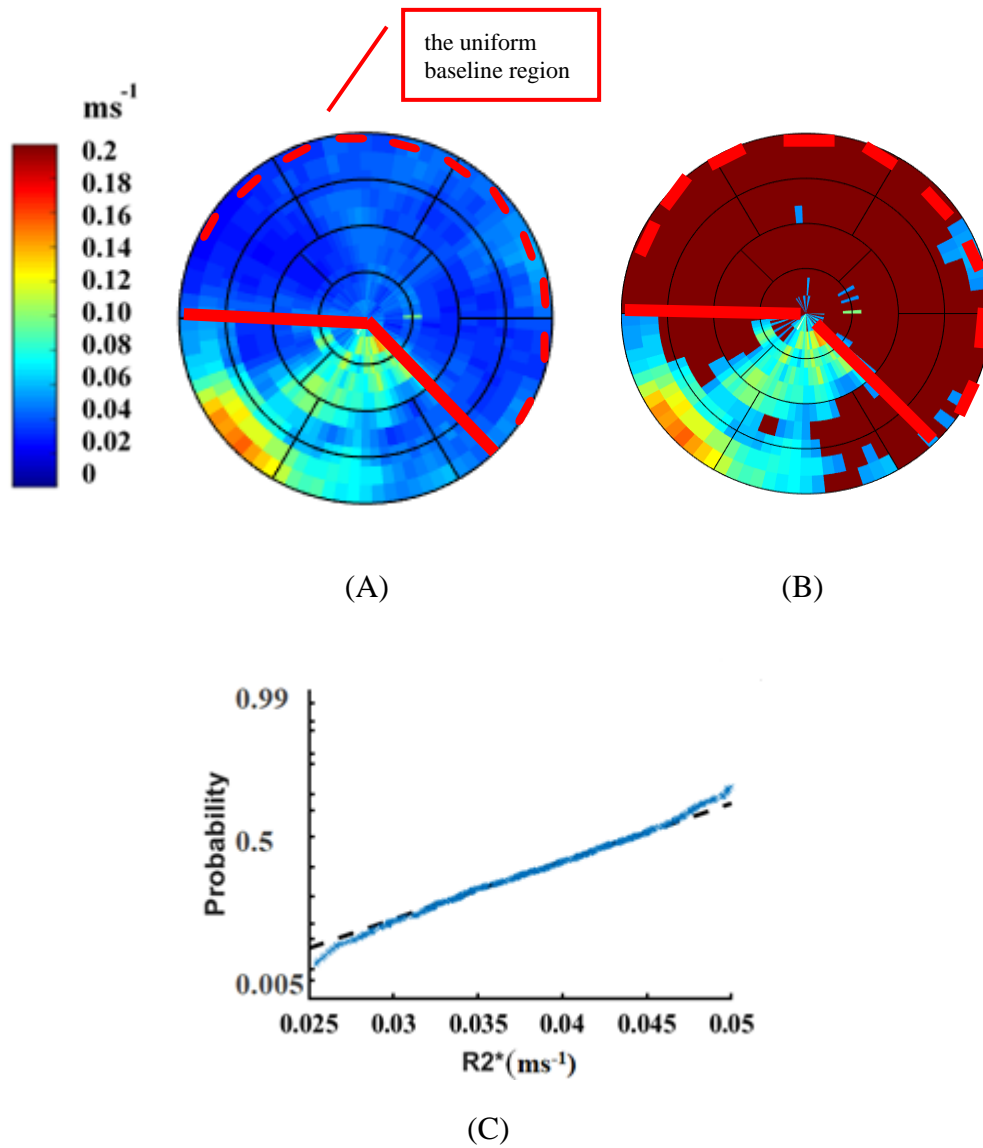
Figure 3. 5. R2* distribution in the region of the LV denoted as a baseline signal. A) The baseline region (ROI outlined in red) was selected based on B) an iterative selection method. C) The selected baseline ROI was interrogated using the Probability plot test and shows an approximately normal distribution of R2* values.

Figure 3.6 provides an analysis of the distribution of R2* values within the same uniform baseline region in individual subjects (C and F). There was a substantive deviation from normality in four dogs (see Appendix D). This variations on R2* distribution might be due to the large slice thickness (6 mm).
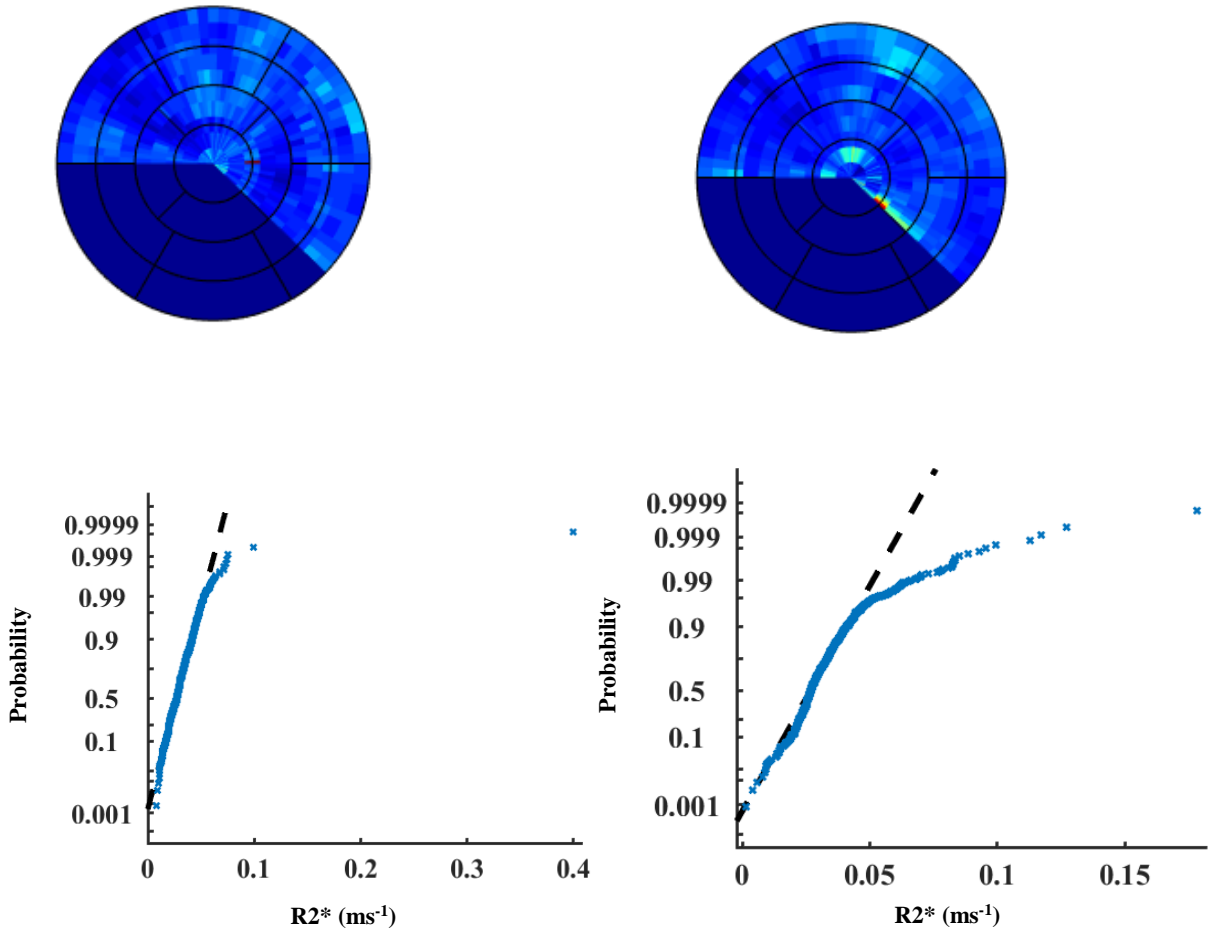
Figure 3. 6. Baseline R2* relaxation rates and their distribution. The upper row shows polar plots of R2*maps covering the entire LV of two dogs (C and F). The lower row shows the distribution of R2* values within the uniform baseline region for these two polar plots. R2* values follow an approximately normal distribution on the left plot but deviate substantially from normality on the right.

Table 3 provides values of the % CV and the 95th percentile of R2* values for each of the six baseline polar plots within the same uniform baseline region (Figure 3.5A). The SNR was higher in dog D compared to other dogs. The baseline T2*-weighted images for this dog were acquired with flip angle 20^0, where T2*-weighted images for the remaining subjects were obtained with flip angle 10^0.

The highest of these (0.08 ms^{-1}) was used as the threshold for differentiating normal R2* regions from abnormally high R2* regions in post-MI polar plots.

Table 3. Comparison of baseline %CV and thresholds based on the 95 percentile

Dog	%CV	95 percentile (ms^{-1})
A	36	0.06
B	40	0.08
C	55	0.05
D	22	0.05
E	36	0.07
F	45	0.06

3.6   Signal decay model for post-MI images

Figure 3.7A shows a representative short axis view of the LV 3 days post-MI with 8 TE values (3-23 ms) demonstrating the T2* signal decay. Figure 3.7B illustrates decay of the ROI signal as a function of echo time. The signal deviates from the exponential curve fitting at late echo times.

TE= 3.4   6.2   8.9   11.8   14.6   17.5   20.3   23.1   ms

(A)

(B)
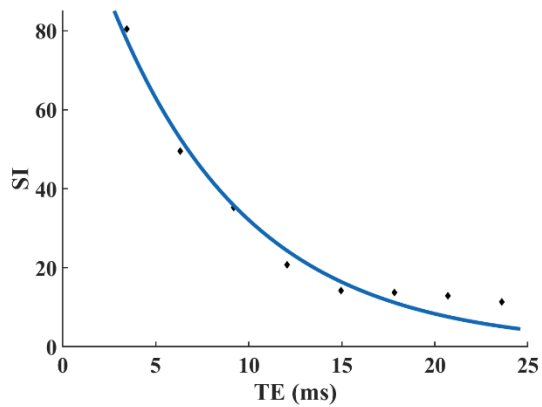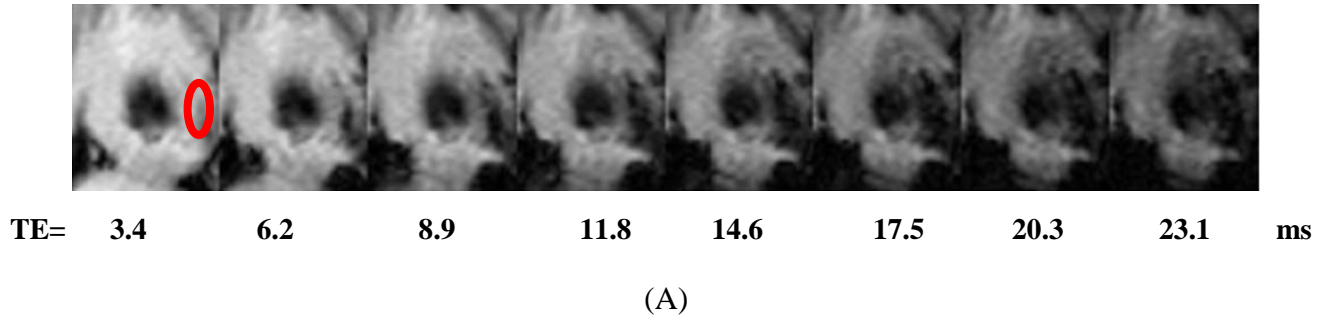
Figure 3.7. Pattern of signal intensity decay post-MI. (A) Panels show the series of short-axis T2*-weighted images of the LV, acquired at 8 echo times. The ROI was selected to cover the core of injury (red). (B) The mono-exponential curve is the best fit for signal intensity (SI) versus TE in the uniform baseline region.

3.7 R2* Analysis for images post-MI

Guided by the baseline analysis, which showed a relatively uniform R2* signal in the lateral, anterior, and septal sectors of the LV (Figure 3.5A), we applied this uniform baseline region to each polar plot obtained post-MI (see appendix E).

In a representative animal at 3 days post-MI, Figure 3.8 shows the R2* maps for each short-axis slice of the entire LV. The respective polar plot (below) identifies regions with non-normal R2*.
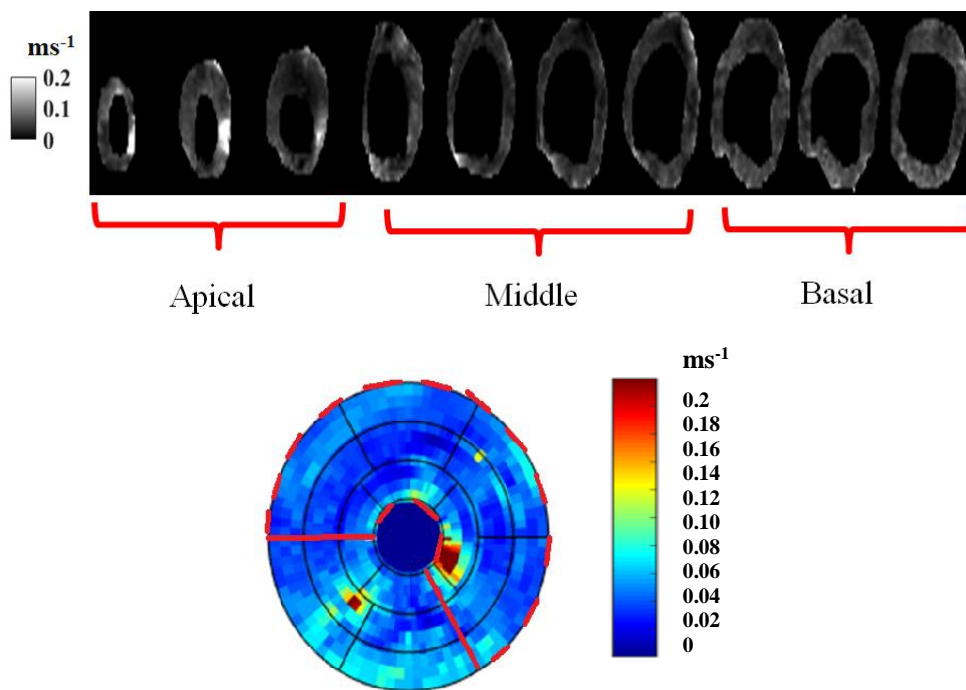
Figure 3. 8. R2* maps of the entire LV post-MI. At day 3 post-MI, ten R2* maps display short-axis slices related to apical, middle, and basal regions of the LV (top) and their corresponding polar plot (bottom). The uniform baseline region is outlined in red, permitting assessment of regions with a non-normal R2* distribution relative to the baseline LV.

Figure3.9A shows the abnormally high R2* within the uniform baseline region and Figure 3.9B shows the segmented abnormally high R2* region based our threshold (R2* > 0.08 ms^{-1}).

(A)   (B)
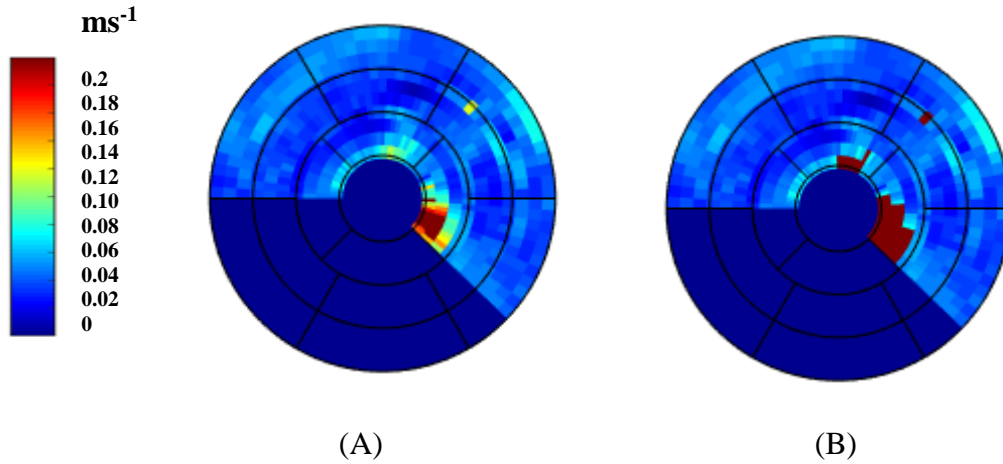
Figure 3. 9. Automatic delineation of the abnormally high R2* region. A) The polar plot of the entire LV at 3 days post-MI excludes the inferior region (blue mask) with relatively high susceptibility artifacts. B) After applying the threshold method, abnormally high R2* regions (in red) are identified based on our threshold.

Figure 3.10 shows the abnormally high R2* based on the literature threshold and our threshold (0.05 ms^{-1} vs. 0.08 ms^{-1}), respectively. Additional results are in Appendix (E).

(A)   (B)
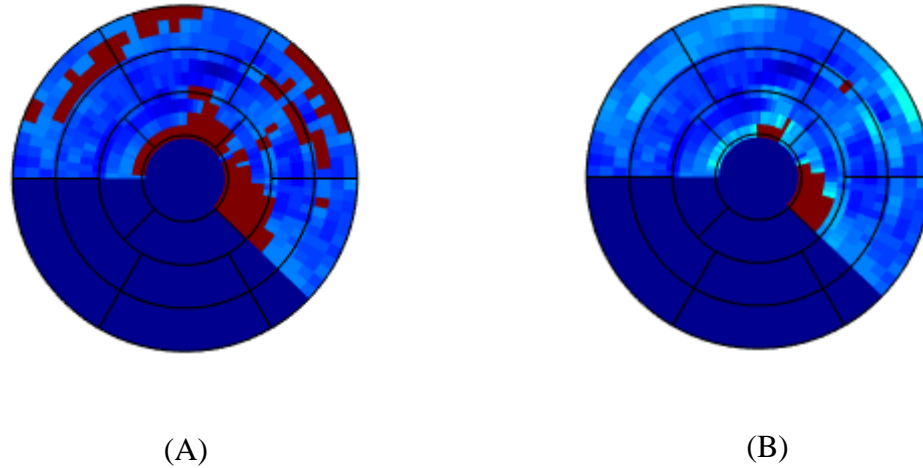
Figure 3. 10. Comparison of the abnormally high R2* region based on the reported and proposed thresholds. The abnormal R2* regions (in red) in the polar plot of the entire LV at 3 days post-MI are identified based on A) a threshold of 0.05 ms^{-1} from the literature and B) a threshold of 0.08 ms^{-1} from our analysis of baseline images.

Changes with time in the mean R2* were significant for day 3 vs. day 41 (p <0.05) for the region with R2* > 0.08 ms^{-1} but not significant for the region with R2* > 0.05 ms^{-1} or for the remote region (Figure 3.11 A). The remote R2* values do not appear to deviate from the baseline value (shown on the vertical axis in Figure 3.11). When we compared R2* values at each time point in the threshold of 0.08 ms^{-1} vs. the corresponding time point in the remote region, there were significant differences (with different levels of significance) between them.

Figure 3.11 B shows the combined evolution of abnormally high R2* regions post-MI. %LV obtained with R2* > 0.05 decreased from 11% at day 3 to 3% at day 41. However, the %LV obtained with the previously reported threshold (R2* > 0.05) indicates 22-42%

involvement of the ROI volume. When we compared %LV at each time point in threshold of 0.08 ms^{-1} vs. the corresponding time point in the threshold of 0.05 ms^{-1}, there were significant differences (with different levels of significance) between them.
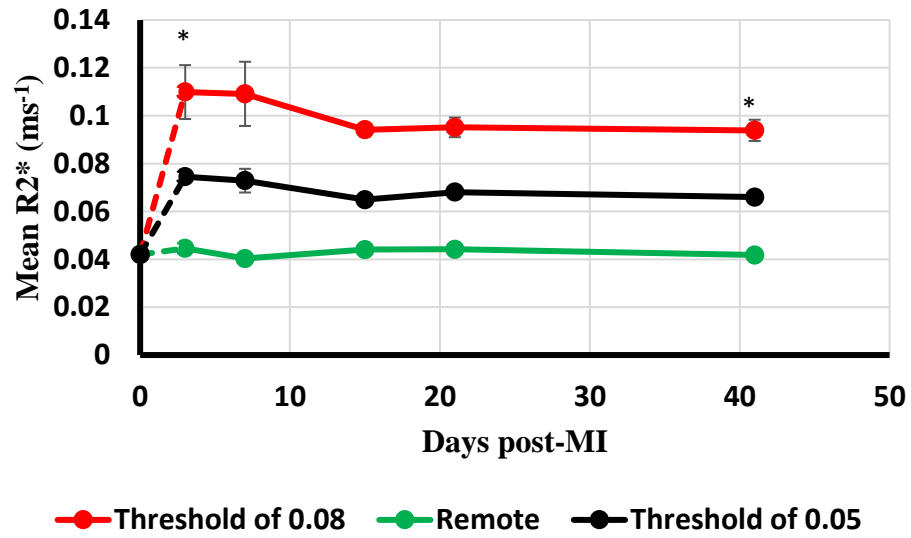
(A)
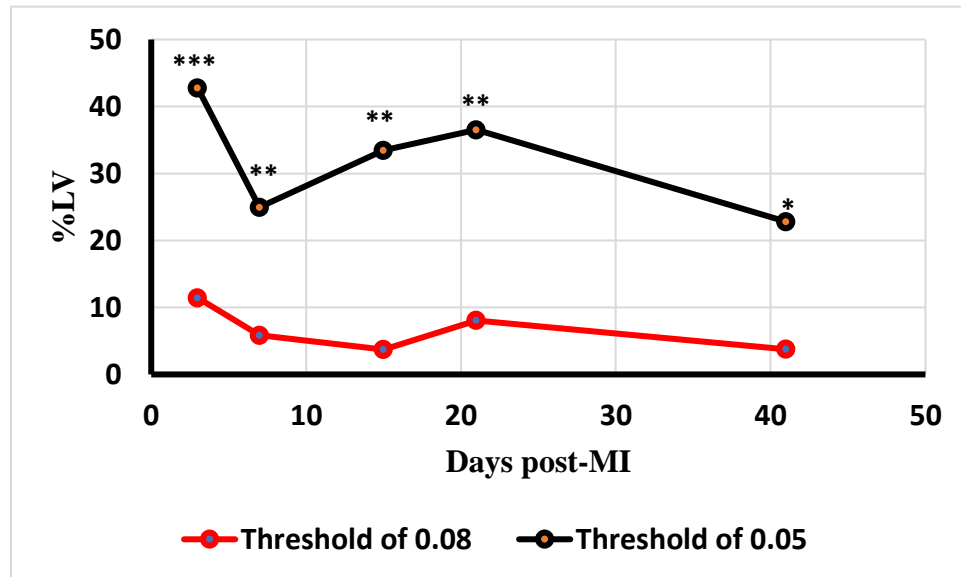
(B)

Figure 3. 11. Analysis of the abnormally high R2* region post-MI. A) Mean R2* values for abnormal regions of myocardium are shown using two different thresholds: 0.05 ms^{-1} (black) and 0.08 ms^{-1} (red), with each mean compared to mean R2* values for remote (normal, unaffected) myocardium (green), averaged over all animals. The two * indicate a significant difference in mean R2* ($p < 0.05$) at day 3 and at day 41 using the 0.08 ms^{-1} threshold and using the 0.05 ms^{-1} threshold. In addition, there were significant differences between the 0.08 ms^{-1} threshold and remote R2* mean values at all data-collection points, including post-MI day 3 ($p < 0.001$), day 8 ($p < 0.001$), day 15 ($p < 0.05$), day 21 ($p < 0.05$) and day 41 ($p < 0.05$). B) The evolving volume of abnormal cardiac tissue (%LV) is graphed over time, post-MI, using the two thresholds: 0.05 ms^{-1} (black) and 0.08 ms^{-1} (red). Depicted are means +/- standard errors for n = 4 dogs. Significant differences between the two thresholds were noted at all data-collection points by mixed model ANOVA ($\alpha = 0.05$): * $p < 0.05$; ** $p < 0.01$; *** $p < 0.001$.

Chapter 4: Discussion, Summary and Future Work

4 Discussion

In CMR imaging, R2* measurements are typically used to identify the presence of hemorrhage. However, various artifacts from different sources can alter the R2* distribution and skew the correspondence between R2* values and noninvasive assessment of the disease process..

Several experimental factors complicate the application of R2* measurements for detecting post-MI changes like hemorrhage. For example, partial volume effects [95, 96], magnetic susceptibility artifacts, low SNR and motion artifacts can influence R2* measurements. Also, the signal decay curve may be restricted from reaching baseline by blood pool and motion artifacts. All these factors can influence calculation of the R2* value.

In studies of iron thalassemia patients, Pennell [93] and Anderson *et al.* [2] indicated that the later TE signals could be buried in blood artifacts and background noise. To address this problem, Westwood *et al.* [97] and Tanner *et al.* [98], also in iron thalassemia studies, adopted a truncation approach in which the images at later TE are subjectively excluded and the remaining signal is fitted with a simple monoexponential model. Importantly, all of these proposed techniques were based on bright-blood T2* acquisition and ROI-based analysis. However, Baksi *et al.* [99] and He *et al.* [100] have shown that when using a dark-blood sequence, the myocardial border is defined clearly and the MRI signals can be properly fitted against all TE values by a monoexponential model.

In pixel-wise technique, R2* measurements are more challenging compared to ROI-based analysis due to low SNR. In a previous report involving black blood T2* mapping in a canine model [101], only images from the first five echoes were included in the fit and it was suggested that this would reduce the impact of motion artifacts. However, in our study excluding the last 2 or 3 echoes in black-blood baseline images did not reduce the fit uncertainty in pixel-wise R2* values (Figure 3.2). Our results indicate that using images from all TE values achieved the lowest standard error in R2* and lowest values of $1 - r^2$. In addition, any changes in the mean R2* values with number of echoes was small. (Table

1). One would expect that under ideal conditions (e.g., no motion artifacts, no contamination from the blood signal) more TE points should provide more precise R2* measurements.

Port and Pomper [102] found that susceptibility artifacts on gradient echo images were moderately reduced with decreasing slice thickness (from 6 mm to 3 mm). This finding fits with our results for healthy human analysis (Table 2). For better visualization of MI, Simonetti *et al.* [103] indicated that the ideal flip angle for inversion-recovery GRE cardiac imaging is 20^0. We found lower %CV in one baseline image with a 20^0 flip angle compared to others with a 10^0 flip angle.

A qualitative study of pig hearts showed that the heart-lung interface or air pockets close to the heart (from the stomach, for example) may potentially cause signal artifacts in T2*-weighted MRI and are distributed radially from the interface [81, 104]. These so-called magnetic susceptibility artifacts are associated with signal loss in T2*-weighted images and therefore increase R2* values. The variations in diamagnetism (e.g., tissue versus air) lead to distortion of the applied magnetic field especially at the interface between tissues (i.e., heart-lung). This field distortion can cause magnetic susceptibility artifacts and affect the distribution of R2* values. Figure 3.3 illustrates the spatial variation in R2* over the entire LV for six dogs in the baseline condition (no MI). It is likely that the high R2* values (red, yellow), which are largely in the inferior septal region are due to magnetic susceptibility-related effects. We expected the variation in R2* values would be highest in the lateral zone due to the susceptibility artifacts produced at the heart-lung interface [81]. But instead, there was low variation in R2* values in this area compared to the inferior-septal region. This result may be due to susceptibility artifacts from air pockets, cardiac veins, or the posterior interventricular branch of the right coronary artery, which could decrease the MR signal detection [104].

The purpose of averaging the six polar plots into one composite polar plot was to identify the regions with relatively low susceptibility artifacts (Figure 3.4 A). The segmental analysis showed variations in R2* values across the LV segments (Figure 3.4 B). R2* variation was at a minimum in the anterior-septal zone. The inferior-septal segments were

51

mostly affected by susceptibility artifacts. The mean R2* value within the uniform baseline region (with expected low susceptibility artifacts) was 0.042 ± 0.01 ms^{-1}, in agreement with the literature [2, 86]. The analysis of the composite polar plot using an iterative selection method (Figure 3.5 A) confirms our observation and segmental analysis, showing that the inferior-septal region is mostly affected by susceptibility artifacts. The distribution of R2* values within the region of relatively low susceptibility artifacts on the cumulative polar plot was approximately normally distributed based on the probability test (Figure 3.5 C), consistent with the results of Kadir *et al.* in 12 patients post-MI [105].

In studies of post-MI T2* imaging, the remote region is located distant from where the infarction injury is believed to be (visually) and away from cardiac veins, so as to avoid susceptibility artifacts [106]. One common approach (R2* > 0.05 ms^{-1}) is based on using the remote region as a reference. In another approach, Kali *et al.*[3] and Bulluck *et al.* [107] defined the hemorrhagic region as the location where the signal intensity on T2*-weighted images is at least 2 SD below a reference region of interest (remote myocardium). They showed that hemorrhagic R2* values range between 0.06-0.07 ms^{-1}. However, with this manual approach two observers are commonly employed to assess inter-observer correspondence and the analysis of multiple-slices over several subjects can be time consuming. Also, image gray level variations, due to variation in B1 and signal detection, make it difficult to use this method over a large region (e.g, whole LV). In addition, Ghugre *et al.*, in a porcine MI-model [63], indicated that the process of LV remodeling post-MI is complicated, with different mechanisms happening concurrently and potentially leading to signal changes in the remote region. Therefore, they suggested that the remote region may not be the recommended choice for reference tissue in MI.

To select the appropriate threshold for detecting abnormal tissue on post-MI images (Table 3), there is a trade-off between underestimating and overestimating the extent of abnormal tissue, where the latter involves including regions with high R2* values due to susceptibility artifacts. The appropriate threshold depends on the MI, the responses post-MI and where the threshold is going to be used. Choosing a higher threshold that results in a low fraction of higher R2* might be a reasonable selection. We have suggested a new

threshold at 3T to estimate the extent of elevated R2* (e.g. hemorrhagic region) post-MI based on the analysis of the distribution of R2* values on baseline images.

In this thesis we considered a novel method for potentially distinguishing normal from abnormal cardiac tissue post-MI. The proposed idea was to use the probability plot procedure to determine a threshold for each post-MI polar plot based on the R2* value at which the data begins to deviate from normality. However, we had to first test this on baseline images to ensure that the area considered to be "abnormal" on these images would be very small. Firstly, we applied an iterative selection algorithm to determine a relatively uniform region within the cumulative baseline R2* polar plot. Within this region, we found that the distribution of R2* values followed an approximately normal distribution based on visual inspection of the probability plot. This was an encouraging result. However, when the probability plot was applied to individual baseline subjects, we found that the distributions for most subjects deviated from normality (Figure 3.6 and Appendix D). For that reason we were unable to apply this novel method to our post-MI data. However, the finding of approximate normality in the cumulative baseline polar plot suggests that it might be possible to further explore this method in the future. In particular, we could determine if improvements to acquisition (e.g., improved shimming) or analysis (other fitting, automated or improved delineation of the myocardium) could improve normality of the R2* distribution in baseline images.

The value of the threshold (R2* > 0.08 ms^{-1}) proposed in this thesis work is in reasonable agreement when compared to the previously reported threshold value (R2* > 0.05 ms^{-1}) for differentiating "normal" from "abnormal" R2* values. However, as shown in Figure 3.9 and Appendix F, the volume of tissue classified as abnormal was substantially smaller with a threshold of 0.08 ms^{-1} compared to 0.05 ms^{-1}. Also, the latter threshold (0.05 ms^{-1}) leads to disconnected abnormal regions (Figure 3.10). Although the reported threshold provides a potential to differentiate between remote and hemorrhagic regions post-MI, there are factors that can cause variation in MRI signals over time points post-MI. For example, hemoglobin byproducts can vary during the healing process. In this regard, Ghugre *et al.*

[63] in a porcine MI model have characterized the form of hemorrhage between day 2 and day 15 post-MI, identifying erythrocytes (containing ferrous iron) as the predominant species at early times post-MI and iron-rich macrophages (with ferric iron) as the predominant species at later times post-MI. Also, the amount of iron present in tissue may be cleared by macrophages through time post-MI.

Several studies have shown that R2* values rose from baseline, and peaked 2 days post-MI followed by a decrease over time post-MI [26, 49, 108]. Ghugre *et al.*[63] in a porcine MI model showed that higher values of R2* post-MI agreed with the presence of both mineralization and hemorrhage, making it a potential marker for those histological characteristics. Moreover, R2* values post-MI did not return to the baseline range, suggesting that elevated R2* may also be associated with the resolution of inflammation and MVO.

In this thesis, the mean values of elevated R2* within the uniform baseline region based on the two thresholds (R2* > 0.08 ms^{-1} and the reported value of R2* > 0.05 ms^{-1}) are compared to remote myocardium averaged over all (n=4) animals (Figure 3.11 A). The mean values of high R2* regions were significantly higher than the mean of remote regions ($p < 0.05$). In addition, the remote regions remained close to the mean R2* of baseline tissue (0.04-0.05 ms^{-1}), consistent with the literature [2, 86]. The evolution of regions with high R2* showed an increase at day 3 relative to the mean baseline value 0.042 ± 0.01 ms^{-1} at day 0, and showed a decrease by day 41 but not a return to remote levels. This might be due to a change in the form of iron, resulting in a change in the magnetic properties [109], or this might be an indication of the degree of iron deposition present in the myocardium [2, 110]. The %LV obtained with an R2* threshold of 0.05 ms^{-1} ranged between 22-42%; whereas, the 95th percentile with threshold of 0.08 ms^{-1} ranged from 3-11% involvement of the ROI volume (Figures 3.11 B).

The time needed for myocardial hemorrhage (one form of high R2*) to resolve is still unclear. Carrick *et al.* [53] studied the time course of both hemorrhage and MVO in patients and demonstrated that hemorrhage only occurred within regions of MVO. The amount of

myocardial hemorrhage was reduced over time post-MI. Robbers *et al.* [43] showed that hemorrhage is a consequence of MVO.

The thesis study has some limitations. First, susceptibility artifacts affect the determination of injury and/or iron in tissue. Our work provides an approximate threshold (0.08 ms^{-1}) to differentiate abnormal (potentially hemorrhagic) tissue, but is based on only six baseline images. Post-MI high R2* values due to susceptibility artifacts could potentially be above this threshold. Second, analysis of the pathophysiology (e.g., mineralization, tissue iron levels) and cardiac measures (e.g., ejection fraction) are required to better understand the consequences of the time course and spatially dependent variation in R2* values post-MI. Third, although previous studies have shown an approximately linear relationship between R2* and tissue iron deposition, other studies indicated that a limited dynamic range for R2* measurements could influence the relationship between measured R2* and iron content [111, 112]. Since the inter-echo time for the first two echoes in our study is approximately 3 ms, we estimate that the highest R2* that could be measured (i.e., the top of the dynamic range) is on the order of $(1/3)$ ms^{-1}. High variations in R2* values could be reduced by increasing the sample size, a limitation of the current study, and would be considered in the next cohort study.

4.1 Summary

R2* mapping procedures are more specific in providing regional and cross-subject comparisons compared to signal intensity measures in individual images. The main goals of this thesis were to assess the R2* signal obtained from cardiac MRI, before and after myocardial infarction in canine subjects. R2* measures are relevant since hemorrhage can be recognized in the presence of other post-MI responses such as edema.

Using all 8 echoes in fitting baseline images led to better goodness of fit and reduced uncertainty compared to using only 5 or 6 echoes and did not lead to substantially different mean R2* over the entire LV. From our assessment of baseline images using polar plots, we found regions of high R2* in the inferior-septal segments of the LV. This is in good agreement with the findings of Sorrel *et al.* (2004) who showed that the presence of susceptibility artifacts in the inferior-septal regions are due to air pockets in adjacent organs, intestine or stomach [104]. Using images from two human volunteers we found that reducing slice thickness led to reduced mean R2* (i.e., thinner slices are better where possible). By using an iterative selection algorithm on a cumulative baseline image, we found a large region (approximately 75% of the LV) with relatively low and uniform R2*. Importantly, the probability plot method showed that the distribution of R2* values in the cumulative polar plot was reasonably close to a normal distribution on visual inspection. However, this normality did not hold for most individual baseline images. Taken together, differences between a cumulative analysis compared to individual analysis, indicate that use of the probability plot for determining thresholds to separate abnormal from healthy tissue post-MI may have potential in the future, but for the present data would likely include (very large) regions of "healthy tissue". We used baseline images to determine a threshold corresponding to the highest percentile (95th) of R2* values for all baseline images. This threshold value (0.08 ms^{-1}) was higher than that previously reported (0.05 ms^{-1}).

We used the large LV region that was found to be relatively uniform on baseline images and both threshold values (0.08 ms^{-1} and 0.05 ms^{-1}) to segment high ("abnormal") R2* regions in post-MI images that had been acquired at several times points (3 to 41 days) post MI. We found much smaller high R2* regions with threshold of 0.08 ms^{-1} compared to 0.05 ms^{-1}. Using the higher threshold, we found that higher R2* values were present in the

inferior-septal and the anterior-lateral regions of the LV. This finding is in agreement with Ghugre *et al.* [63] and Kali *et al.* [3] who showed higher R2* values in post-MI images of the anterior-lateral region due to LAD occlusion. However, our findings on high R2* values in the inferior-septal region is not consistent with other human and animal studies [83–85]; this discrepancy could be due to either susceptibility artifacts or LAD occlusion. We found that mean R2* values of remote tissue regions remained in the range of the mean R2* of baseline tissue, which is consistent with previous reports [2, 86, 87]. In addition, evolution of R2* post-MI showed an increase at day 3 relative to the mean baseline value and a decrease on day 41 but did not return to baseline levels. As well, the percentage of abnormal tissue within the uniform baseline region of the LV (%LV) reached a maximum level at day 3 and generally decreased by day 41.

4.2 Future Work

One of the major challenges of R2* mapping involves the contribution of macroscopic magnetic field variations to R2* often due to interfaces between regions of different magnetic susceptibility (sometimes called susceptibility artifacts). We found that this was a major contribution to R2* in baseline images (inferior-septal region of LV). There are several methods that could potentially reduce the contribution of susceptibility artifacts to R2*. For example, improved shimming of the heart [113] may be considered. In addition, reducing slice thickness reduces the susceptibility contribution [114], but also reduces the signal to noise ratio and would increase the number of breath holds required. To reduce the number of breath holds, perhaps increasing parallel imaging acceleration would be helpful, again at expense of SNR. An improved multi-channel RF coil could potentially be of benefit to increase SNR. Post-processing methods could also be helpful to reduce susceptibility artifact contribution. For example, a more complex fit model that includes a Gaussian-like component as well as an exponential-like component could be used but requires good SNR. We have performed preliminary experiments with this approach, but it failed possibly due to inadequate SNR. In the future, we could filter images first before attempting this fitting procedure. Also, phase maps (from the same sequence) could possibly be used to help correct for susceptibility contributions. Reducing the contribution from susceptibility artifacts may also improve the possibility of using the probability plot analysis.

A reliable and accurate segmentation method for the LV wall boundary would be valuable. This might enhance the potential of the probability plot thresholding method to produce precise quantification of hemorrhagic cores in the entire LV, decrease the user involvement and improve the time required for image analysis to be performed.

It is also important to incorporate R2* mapping (i.e. high R2* regions) with 2D or 3D late gadolinium images in order to assess the hemorrhage location with respect to microvascular obstruction. This would require image registration between the two-dimensional multislice T2*-weighted images and 3D gadolinium-enhanced images.

It may also be beneficial to correlate the appearance of a hypointense zone on other relaxation parameters such as the T1 and T2 maps with R2* maps to define the region of myocardial hemorrhage [107]. In addition, hybrid imaging (PET/MRI) may give metabolic information about myocardial tissue that can establish the best strategy for myocardial hemorrhage evaluation and illustrate its temporal evolution [115]. Furthermore, variations in functional cardiac measures (i.e., ejection fraction) provide important information regarding infarct size [116], which in turn determines the degree of myocardial hemorrhage [45]. Finally, histopathologic images are necessary to localize the hemorrhagic core within the infarcted region and iron deposition within the hemorrhagic zone [117].

The human heart is similar to the canine heart in structure and equivalent in function. However, in any model, susceptibility artifacts should be minimized, for example, using thinner slice thickness or improving heart shimming. The R2* thresholding approach can be translated to human MI studies by showing the relation between R2* threshold and impaired ventricular functions (i.e., ejection fraction).

4.3 Conclusion:

In this thesis, we found that R2* maps of the LV of canine subjects that had not been exposed to heart injury (baseline) showed a region of very high R2* values, likely associated with magnetic susceptibility artifact, in the inferior-septal region of the LV. Eliminating latter echoes in the fitting procedure did not reduce this artifact and led to reduced goodness of fit and increased fit uncertainty for R2*. However, based on our studies on human subjects we found reduced mean R2* with thinner slices (4 mm vs 6 mm) suggesting reduced susceptibility artifact.

In addressing our first objective, we found a large LV region on baseline images that had relatively low and uniform R2*. From the analysis of this region as proposed in our second objective, we determined that a threshold R2* value of approximately 0.08 ms^{-1} would be reasonable for separating normal from "abnormal" tissue post-MI, within this spatial location. This threshold is higher than that (0.05 ms^{-1}) previously reported in animal and clinical studies. By considering this selected region on the post-MI polar plots, as per our third objective, we found that segmented volumes of "abnormal" tissue with our threshold were much smaller than regions segmented with the previously reported threshold. Mean R2* values of remote tissue regions remained in the range of the mean R2* of baseline tissue. Also, the mean values of high R2* regions were significantly higher than the mean of remote regions ($p < 0.05$) over time post-MI. In addition, the %LV with our R2* threshold 0.08 ms^{-1} ranged between 3-11%.

References:

[1]   "Health Fact Sheets The 10 leading causes of death, 2012," *Statistics Canada*, 2015. [Online]. Available: https://www150.statcan.gc.ca/n1/pub/82-625-x/2015001/article/14296-eng.htm.

[2]   L. J. Anderson, S. Holden, B. Davis, E. Prescott, C. C. Charrier, N. H. Bunce, D. N. Firmin, B. Wonke, J. Porter, J. M. Walker, and D. J. Pennell, "Cardiovascular T2-star (T2*) magnetic resonance for the early diagnosis of myocardial iron overload," *Eur. Heart J.*, vol. 22, no. 23, pp. 2171–2179, 2001.

[3]   A. Kali, R. L. Tang, A. Kumar, J. K. Min, and R. Dharmakumar, "Detection of acute reperfusion myocardial hemorrhage with cardiac MR imaging: T2 versus T2," *Radiology*, vol. 269, no. 2, pp. 387–395, Nov. 2013.

[4]   "Heart Anatomy," *Texas Heart Institute*. [Online]. Available: https://www.texasheart.org/heart-health/heart-information-center/topics/heart-anatomy/.

[5]   K. Mani and R. N. Kitsis, "Myocyte apoptosis: Programming ventricular remodeling," *J. Am. Coll. Cardiol.*, vol. 41, no. 5, pp. 761–764, Mar. 2003.

[6]   A. K. Peter, M. A. Bjerke, and L. A. Leinwand, "Biology of the cardiac myocyte in heart disease," *Mol. Biol. Cell*, vol. 27, no. 14, pp. 2149–2160, Jul. 2016.

[7]   P. A. Iaizzo, *Handbook of cardiac anatomy, physiology, and devices, third edition*. Cham: Springer International Publishing, 2015.

[8]   A. Manzo, Y. Ootaki, C. Ootaki, K. Kamohara, and K. Fukamachi, "Comparative study of heart rate variability between healthy human subjects and healthy dogs, rabbits and calves," *Lab. Anim.*, vol. 43, no. 1, pp. 41–45, Jan. 2009.

[9]   "Your Heart & Blood Vessels," *Cleveland Clinic*, 2018. [Online]. Available: https://my.clevelandclinic.org/health/articles/17057-your-heart--blood-vessels.

[10]   A. Goldberger, Ary Louis; Goldberger, Zachary D; Shvilkin, *Goldberger's clinical electrocardiography: a simplified approach*, 8th ed. Elsevier/Saunders, 2013.

[11]   R. S. Wright, J. L. Anderson, C. D. Adams, C. R. Bridges, D. E. Casey, S. M. Ettinger, F. M. Fesmire, T. G. Ganiats, H. Jneid, A. M. Lincoff, E. D. Peterson, G. J. Philippides, P. Theroux, N. K. Wenger, and J. P. Zidar, "2011 ACCF/AHA Focused Update Incorporated Into the ACC/AHA 2007 Guidelines for the Management of Patients With Unstable Angina/Non–ST-Elevation Myocardial Infarction," *J. Am. Coll. Cardiol.*, vol. 57, no. 19, pp. e215–e367, May 2011.

[12]   R. Virmani, F. D. Kolodgie, A. P. Burke, A. Farb, and S. M. Schwartz, "Lessons from sudden coronary death: A comprehensive morphological classification scheme for atherosclerotic lesions," *Arterioscler. Thromb. Vasc. Biol.*, vol. 20, no. 5, pp. 1262–1275, May 2000.

[13]   K. A. Reimer and R. B. Jennings, "The 'wavefront phenomenon' of myocardial ischemic cell death. II. Transmural progression of necrosis within the framework of ischemic bed size (myocardium at risk) and collateral flow.," *Lab. Invest.*, vol. 40, no. 6, pp. 633–44, 1979.

[14]   G. Vandeplassche, C. Hermans, J. Van Haecke, L. Wouters, M. Borgers, and W. Flameng, "Evaluation of factors influencing myocardial infarct size in unconscious dogs," *Cardiovasc. Res.*, vol. 25, no. 10, pp. 844–854, Oct. 1991.

[15]   Y. T. Shen, J. T. Fallon, M. Iwase, and S. F. Vatner, "Innate protection of baboon myocardium: effects of coronary artery occlusion and reperfusion.," *Am. J. Physiol.*, vol. 270, no. 5, pp. H1812–H1818, 1996.

[16]   Y. T. Shen, D. R. Knight, S. F. Vatner, W. C. Randall, and J. X. Thomas Jr., "Responses to coronary artery occlusion in conscious dogs with selective cardiac denervation," *Am J Physiol*, vol. 255, no. 3 Pt 2, pp. H525-33, 1988.

[17]   G. Heusch, "Myocardial Ischemia: Lack of Coronary Blood Flow or Myocardial Oxygen Supply/Demand Imbalance?," *Circ. Res.*, vol. 119, no. 2, pp. 194–196, Jul. 2016.

[18] D. M. Yellon and D. J. Hearse, "Determinants of infarct size during permanent occlusion of a coronary artery in the closed chest dog," *J. Am. Coll. Cardiol.*, vol. 9, no. 3, pp. 647–654, Mar. 1987.

[19] K. A. Reimer, R. B. Jennings, F. R. Cobb, R. H. Murdock, J. C. Greenfield, L. C. Becker, B. H. Bulkley, G. M. Hutchins, R. P. Schwartz, and K. R. Bailey, "Animal Models for protecting ischemic myocardium: Results of the NHLBI cooperative study. Comparison of unconscious and conscious dog models," *Circ. Res.*, vol. 56, no. 5, pp. 651–665, 1985.

[20] F. Van De Werf, J. Bax, A. Betriu, C. Blomstrom-Lundqvist, F. Crea, V. Falk, G. Filippatos, K. Fox, K. Huber, A. Kastrati, A. Rosengren, P. G. Steg, M. Tubaro, F. Verheugt, F. Weidinger, M. Weis, A. Vahanian, J. Camm, R. De Caterina, V. Dean, K. Dickstein, C. Funck-Brentano, I. Hellemans, S. D. Kristensen, K. McGregor, U. Sechtem, S. Silber, M. Tendera, P. Widimsky, J. L. Zamorano, F. V. Aguirre, N. Al-Attar, E. Alegria, F. Andreotti, W. Benzer, O. Breithardt, N. Danchin, C. Di Mario, D. Dudek, D. Gulba, S. Halvorsen, P. Kaufmann, R. Kornowski, G. Y. H. Lip, and F. Rutten, "Management of acute myocardial infarction in patients presenting with persistent ST-segment elevation," *Eur. Heart J.*, vol. 29, no. 23, pp. 2909–2945, Dec. 2008.

[21] D. M. Yellon and D. J. Hausenloy, "Myocardial Reperfusion Injury," *N. Engl. J. Med.*, 2007.

[22] R. B. Jennings, J. Schaper, M. L. Hill, C. Steenbergen, and K. A. Reimer, "Effect of reperfusion late in the phase of reversible ischemic injury. Changes in cell volume, electrolytes, metabolites, and ultrastructure," *Circ. Res.*, vol. 56, no. 2, pp. 262–278, Feb. 1985.

[23] K. C. Wu, E. A. Zerhouni, R. M. Judd, C. H. Lugo-Olivieri, L. A. Barouch, S. P. Schulman, R. S. Blumenthal, and J. A. C. Lima, "Prognostic significance of microvascular obstruction by magnetic resonance imaging in patients with acute myocardial infarction," *Circulation*, vol. 97, no. 8, pp. 765–772, Mar. 1998.

[24] M. C. Fishbein, J. Y-Rit, U. Lando, K. Kanmatsuse, J. C. Mercier, and W. Ganz,

"The relationship of vascular injury and myocardial hemorrhage to necrosis after reperfusion," *Circulation*, vol. 62, no. 6 I, pp. 1274–1279, Dec. 1980.

[25] R. Symons, P. G. Masci, K. Goetschalckx, K. Doulaptsis, S. Janssens, and J. Bogaert, "Effect of Infarct Severity on Regional and Global Left Ventricular Remodeling in Patients with Successfully Reperfused ST Segment Elevation Myocardial Infarction," *Radiology*, vol. 274, no. 1, pp. 93–102, Jan. 2015.

[26] A. M. Beek, R. Nijveldt, and A. C. Van Rossum, "Intramyocardial hemorrhage and microvascular obstruction after primary percutaneous coronary intervention," *Int. J. Cardiovasc. Imaging*, vol. 26, no. 1, pp. 49–55, Jan. 2010.

[27] O. Husser, J. V. Monmeneu, J. Sanchis, J. Nunez, M. P. Lopez-Lereu, C. Bonanad, F. Chaustre, C. Gomez, M. J. Bosch, R. Hinarejos, F. J. Chorro, G. A. J. Riegger, A. Llacer, and V. Bodi, "Cardiovascular magnetic resonance-derived intramyocardial hemorrhage after STEMI: Influence on long-term prognosis, adverse left ventricular remodeling and relationship with microvascular obstruction," *Int. J. Cardiol.*, vol. 167, no. 5, pp. 2047–2054, Sep. 2013.

[28] I. Eitel, K. Kubusch, O. Strohm, S. Desch, Y. Mikami, S. De Waha, M. Gutberlet, G. Schuler, M. G. Friedrich, and H. Thiele, "Prognostic value and determinants of a hypointense infarct core in T2-weighted cardiac magnetic resonance in acute reperfused ST-elevation- myocardial infarction," *Circ. Cardiovasc. Imaging*, vol. 4, no. 4, pp. 354–362, Jul. 2011.

[29] R. A. Kloner, C. E. Ganote, and R. B. Jennings, "The 'no reflow' phenomenon after temporary coronary occlusion in the dog," *J. Clin. Invest.*, vol. 54, no. 6, pp. 1496–1508, Dec. 1974.

[30] E. Braunwald and R. A. Kloner, "Myocardial reperfusion: A double-edged sword?," *J. Clin. Invest.*, vol. 76, no. 5, pp. 1713–1719, Nov. 1985.

[31] C. Bouleti, T. Mathivet, B. Coqueran, J. M. Serfaty, M. Lesage, E. Berland, C. Ardidie-Robouant, G. Kauffenstein, D. Henrion, B. Lapergue, M. Mazighi, C. Duyckaerts, G. Thurston, D. M. Valenzuela, A. J. Murphy, G. D. Yancopoulos, C.

Monnot, I. Margaill, and S. Germain, "Protective effects of angiopoietin-like 4 on cerebrovascular and functional damages in ischaemic stroke," *Eur. Heart J.*, vol. 34, no. 47, pp. 3657–3668, Dec. 2013.

[32] A. Galaup, E. Gomez, R. Souktani, M. Durand, A. Cazes, C. Monnot, J. Teillon, S. Le Jan, C. Bouleti, G. Briois, J. Philippe, S. Pons, V. Martin, R. Assaly, P. Bonnin, P. Ratajczak, A. Janin, G. Thurston, D. M. Valenzuela, A. J. Murphy, G. D. Yancopoulos, R. Tissier, A. Berdeaux, B. Ghaleh, and S. Germain, "Protection against myocardial infarction and no-reflow through preservation of vascular integrity by angiopoietin-like 4," *Circulation*, vol. 125, no. 1, pp. 140–149, Jan. 2012.

[33] H. Arheden, "Intramyocardial hemorrhage in acute myocardial infarction: Prognostic biomarker and treatment target?," *Circ. Cardiovasc. Imaging*, vol. 9, no. 1, Jan. 2016.

[34] N. R. Ghugre, M. Pop, J. Barry, K. A. Connelly, and G. A. Wright, "Quantitative magnetic resonance imaging can distinguish remodeling mechanisms after acute myocardial infarction based on the severity of ischemic insult," *Magn. Reson. Med.*, vol. 70, no. 4, pp. 1095–1105, Oct. 2013.

[35] A. K. M. T. Zaman, C. J. French, J. L. Spees, A. S. Binbrek, and B. E. Sobel, "Vascular rhexis in mice subjected to non-sustained myocardial ischemia and its therapeutic implications," *Exp. Biol. Med.*, vol. 236, no. 5, pp. 598–603, May 2011.

[36] A. Kali, I. Cokic, R. Tang, A. Dohnalkova, L. Kovarik, H.-J. Yang, A. Kumar, F. S. Prato, J. C. Wood, D. Underhill, E. Marbán, and R. Dharmakumar, "Persistent Microvascular Obstruction After Myocardial Infarction Culminates in the Confluence of Ferric Iron Oxide Crystals, Proinflammatory Burden, and Adverse Remodeling," *Circ. Cardiovasc. Imaging*, vol. 9, no. 11, Nov. 2016.

[37] J. Ganame, G. Messalli, S. Dymarkowski, F. E. Rademakers, W. Desmet, F. Van De Werf, and J. Bogaert, "Impact of myocardial haemorrhage on left ventricular function and remodelling in patients with reperfused acute myocardial infarction,"

Eur. Heart J., vol. 30, no. 12, pp. 1440–1449, Jun. 2009.

[38] D. P. O'Regan, R. Ahmed, N. Karunanithy, C. Neuwirth, Y. Tan, G. Durighel, J. V. Hajnal, I. Nadra, S. J. Corbett, and S. A. Cook, "Reperfusion Hemorrhage Following Acute Myocardial Infarction: Assessment with T2* Mapping and Effect on Measuring the Area at Risk," *Radiology*, vol. 250, no. 3, pp. 916–922, Mar. 2009.

[39] R. H. Hashemi, W. G. Bradley, and C. J. Lisanti, *MRI: The Basics: The Basics*, 3rd ed. Philadelphia : Wolters Kluwer Health, 2012.

[40] J. P. Ridgway, "Cardiovascular magnetic resonance physics for clinicians: part I," *J. Cardiovasc. Magn. Reson.*, vol. 12, no. 1, p. 71, 2010.

[41] P. V. Prasad, Ed., *Magnetic Resonance Imaging: Methods and Biologic Applications*. Springer Science & Business Media, 2006.

[42] R. B. Driesen, J. Zalewski, N. Vanden Driessche, K. Vermeulen, J. Bogaert, K. R. Sipido, F. Van De Werf, and P. Claus, "Histological correlate of a cardiac magnetic resonance imaged microvascular obstruction in a porcine model of ischemia-reperfusion," *Cardiovasc. Pathol.*, vol. 21, no. 3, pp. 129–131, May 2012.

[43] L. F. H. J. Robbers, E. S. Eerenberg, P. F. A. Teunissen, M. F. Jansen, M. R. Hollander, A. J. G. Horrevoets, P. Knaapen, R. Nijveldt, M. W. Heymans, M. M. Levi, A. C. Van Rossum, H. W. M. Niessen, C. B. Marcu, A. M. Beek, and N. Van Royen, "Magnetic resonance imaging-defined areas of microvascular obstruction after acute myocardial infarction represent microvascular destruction and haemorrhage," *Eur. Heart J.*, vol. 34, no. 30, pp. 2346–2353, Aug. 2013.

[44] S. F. Pedersen, S. A. Thrysøe, M. P. Robich, W. P. Paaske, S. Ringgaard, H. E. Bøtker, E. S. S. Hansen, and W. Y. Kim, "Assessment of intramyocardial hemorrhage by T1-weighted cardiovascular magnetic resonance in reperfused acute myocardial infarction," *J. Cardiovasc. Magn. Reson.*, vol. 14, no. 1, p. 59, 2012.

[45] A. Kumar, J. D. Green, J. M. Sykes, P. Ephrat, J. J. L. Carson, A. J. Mitchell, G. Wisenberg, and M. G. Friedrich, "Detection and quantification of myocardial reperfusion hemorrhage Using T2 (*)-weighted CMR," *JACC Cardiovasc. Imaging*, vol. 4, no. 12, pp. 1274–1283, Dec. 2011.

[46] J. M. Gomori and R. I. Grossman, "Mechanisms responsible for the MR appearance and evolution of intracranial hemorrhage.," *RadioGraphics*, vol. 8, no. 3, pp. 427–440, May 1988.

[47] J. M. Gomori, R. I. Grossman, C. Yu-Ip, and T. Asakura, "NMR relaxation times of blood: Dependence on field strength, oxidation state, and cell integrity," *J. Comput. Assist. Tomogr.*, vol. 11, no. 4, pp. 684–690, Jul. 1987.

[48] W. G. Bradley, "MR appearance of hemorrhage in the brain.," *Radiology*, vol. 189, no. 1, pp. 15–26, Oct. 1993.

[49] D. P. O'Regan, B. Ariff, C. Neuwirth, Y. Tan, G. Durighel, and S. A. Cook, "Assessment of severe reperfusion injury with T2* cardiac MRI in patients with acute myocardial infarction," *Heart*, vol. 96, no. 23, pp. 1885–1891, Dec. 2010.

[50] C. Basso, F. Corbetti, C. Silva, A. Abudureheman, C. Lacognata, L. Cacciavillani, G. Tarantini, M. P. Marra, A. Ramondo, G. Thiene, and S. Iliceto, "Morphologic Validation of Reperfused Hemorrhagic Myocardial Infarction by Cardiovascular Magnetic Resonance," *Am. J. Cardiol.*, vol. 100, no. 8, pp. 1322–1327, Oct. 2007.

[51] C. S. Lotan, S. K. Miller, G. B. Cranney, G. M. Pohost, and G. A. Elgavish, "The effect of postinfarction intramyocardial hemorrhage on transverse relaxation time," *Magn. Reson. Med.*, vol. 23, no. 2, pp. 346–355, Feb. 1992.

[52] C. S. Lotan, A. Bouchard, G. B. Cranney, S. P. Bishop, and G. M. Pohost, "Assessment of postreperfusion myocardial hemorrhage using proton NMR imaging at 1.5 T," *Circulation*, vol. 86, no. 3, pp. 1018–1025, Sep. 1992.

[53] D. Carrick, C. Haig, N. Ahmed, M. McEntegart, M. C. Petrie, H. Eteiba, S. Hood, S. Watkins, M. M. Lindsay, A. Davie, A. Mahrous, I. Mordi, S. Rauhalammi, N. Sattar, P. Welsh, A. Radjenovic, I. Ford, K. G. Oldroyd, and C. Berry,

"Myocardial hemorrhage after acute reperfused ST-segment-elevation myocardial infarction: Relation to microvascular obstruction and prognostic significance," *Circ. Cardiovasc. Imaging*, vol. 9, no. 1, Jan. 2016.

[54] J. S. Hankins, M. B. McCarville, R. B. Loeffler, M. P. Smeltzer, M. Onciu, F. A. Hoffer, C. S. Li, W. C. Wang, R. E. Ware, and C. M. Hillenbrand, "R2* magnetic resonance imaging of the liver in patients with iron overload," *Blood*, vol. 113, no. 20, pp. 4853–4855, May 2009.

[55] D. Stark, N. Bass, A. Moss, and B. Bacon, "Nuclear magnetic resonance imaging of experimentally induced liver disease.," *Radiology*, vol. 148, no. 3, pp. 743–751, Sep. 1983.

[56] R. Engelhardt, J. H. Langkowski, R. Fischer, P. Nielsen, H. Kooijman, H. C. Heinrich, and E. Bücheler, "Liver iron quantification: Studies in aqueous iron solutions, iron overloaded rats, and patients with hereditary hemochromatosis," *Magn. Reson. Imaging*, vol. 12, no. 7, pp. 999–1007, Jan. 1994.

[57] Z. J. Wang, J. C. Haselgrove, M. B. Martin, A. M. Hubbard, S. Li, K. Loomes, J. R. Moore, H. Zhao, and A. R. Cohen, "Evaluation of iron overload by single voxel MRS measurement of liver T2," *J. Magn. Reson. Imaging*, vol. 15, no. 4, pp. 395–400, Apr. 2002.

[58] R. M. Dixon, P. Styles, F. N. Al-Refaie, G. J. Kemp, S. M. Donohue, B. Wonke, A. V. Hoffbrand, G. K. Radda, and B. Rajagopalan, "Assessment of hepatic iron overload in thalassemic patients by magnetic resonance spectroscopy," *Hepatology*, vol. 19, no. 4, pp. 904–910, Apr. 1994.

[59] J. P. Kaltwasser, R. Gottschalk, K. P. Schalk, and W. Hartl, "Non-invasive quantitation of liver iron-overload by magnetic resonance imaging," *Br. J. Haematol.*, vol. 74, no. 3, pp. 360–363, Mar. 1990.

[60] S. I. Mavrogeni, E. D. Gotsis, V. Markussis, N. Tsekos, C. Politis, E. Vretou, and D. Kremastinos, "T2 relaxation time study of iron overload in b-thalassemia," *Magn. Reson. Mater. Physics, Biol. Med.*, vol. 6, no. 1, pp. 7–12, Aug. 1998.

[61] N. R. Ghugre, C. M. Enriquez, I. Gonzalez, M. D. Nelson, T. D. Coates, and J. C. Wood, "MRI detects myocardial iron in the human heart," *Magn. Reson. Med.*, vol. 56, no. 3, pp. 681–686, Sep. 2006.

[62] D. Kandler, C. Lücke, M. Grothoff, C. Andres, L. Lehmkuhl, S. Nitzsche, F. Riese, M. Mende, S. de Waha, S. Desch, P. Lurz, I. Eitel, and M. Gutberlet, "The relation between hypointense core, microvascular obstruction and intramyocardial haemorrhage in acute reperfused myocardial infarction assessed by cardiac magnetic resonance imaging," *Eur. Radiol.*, vol. 24, no. 12, pp. 3277–3288, Dec. 2014.

[63] N. R. Ghugre, V. Ramanan, M. Pop, Y. Yang, J. Barry, B. Qiang, K. A. Connelly, A. J. Dick, and G. A. Wright, "Quantitative tracking of edema, hemorrhage, and microvascular obstruction in subacute myocardial infarction in a porcine model by MRI," *Magn. Reson. Med.*, vol. 66, no. 4, pp. 1129–1141, Oct. 2011.

[64] K. A. Miszkiel, M. N. J. Paley, I. D. Wilkinson, M. A. Hall-Craggs, R. Ordidge, B. E. Kendall, R. F. Miller, and M. J. G. Harrison, "The measurement of R2, R2 and R2' in HIV-infected patients using the prime sequence as a measure of brain iron deposition," *Magn. Reson. Imaging*, vol. 15, no. 10, pp. 1113–1119, Jan. 1997.

[65] A. Kidambi and S. Plein, "Detection of intramyocardial haemorrhage by MRI—no single rule," *Nat. Rev. Cardiol.*, vol. 12, no. 4, pp. 198–198, Apr. 2015.

[66] M. D. Cerqueira, N. J. Weissman, V. Dilsizian, A. K. Jacobs, S. Kaul, W. K. Laskey, D. J. Pennell, J. A. Rumberger, T. Ryan, and M. S. Verani, "Standardized myocardial sementation and nomenclature for tomographic imaging of the heart: A Statement for Healthcare Professionals from the Cardiac Imaging Committee of the Council on Clinical Cardiology of the American Heart Association," *Circulation*, vol. 105, no. 4, pp. 539–542, Jan. 2002.

[67] P. Donato, P. Coelho, C. Santos, A. Bernardes, and F. Caseiro-Alves, "Correspondence between left ventricular 17 myocardial segments and coronary anatomy obtained by multi-detector computed tomography: An ex vivo contribution," *Surg. Radiol. Anat.*, vol. 34, no. 9, pp. 805–810, Nov. 2012.

[68]   O. Pereztol-Valdés, J. Candell-Riera, C. Santana-Boado, J. Angel, S. Aguadé-Bruix, J. Castell-Conesa, E. V. Garcia, and J. Soler-Soler, "Correspondence between left ventricular 17 myocardial segments and coronary arteries," *Eur. Heart J.*, vol. 26, no. 24, pp. 2637–2643, Dec. 2005.

[69]   J. T. Ortiz-Pérez, J. Rodríguez, S. N. Meyers, D. C. Lee, C. Davidson, and E. Wu, "Correspondence Between the 17-Segment Model and Coronary Arterial Anatomy Using Contrast-Enhanced Cardiac Magnetic Resonance Imaging," *JACC Cardiovasc. Imaging*, vol. 1, no. 3, pp. 282–293, May 2008.

[70]   P. A. Cain, M. Ugander, J. Palmer, M. Carlsson, E. Heiberg, and H. Arheden, "Quantitative polar representation of left ventricular myocardial perfusion, function and viability using SPECT and cardiac magnetic resonance: Initial results," *Clin. Physiol. Funct. Imaging*, vol. 25, no. 4, pp. 215–222, Jul. 2005.

[71]   M. D. Cerqueira, N. J. Weissman, V. Dilsizian, A. K. Jacobs, S. Kaul, W. K. Laskey, D. J. Pennell, J. A. Rumberger, T. Ryan, and M. S. Verani, "Standardized myocardial sementation and nomenclature for tomographic imaging of the heart: A Statement for Healthcare Professionals from the Cardiac Imaging Committee of the Council on Clinical Cardiology of the American Heart Association," *Circulation*, vol. 105, no. 4, pp. 539–542, Mar. 2002.

[72]   W. S. Cleveland and R. McGill, "Graphical perception and graphical methods for analyzing scientific data," *Science (80-.).*, vol. 229, no. 4716, pp. 828–833, 1985.

[73]   J. J. Filliben, "The probability plot correlation coefficient test for normality," *Technometrics*, vol. 17, no. 1, pp. 111–117, Feb. 1975.

[74]   J. M. Chambers, W. S. Cleveland, B. Kleiner, and P. A. Tukey, *Graphical Methods for Data Analysis*. 1983.

[75]   K. C. Wu, "CMR of microvascular obstruction and hemorrhage in myocardial infarction," *J. Cardiovasc. Magn. Reson.*, vol. 14, no. 1, p. 68, 2012.

[76]   L. A. J. Higginson, F. White, H. A. Heggtveit, T. M. Sanders, C. M. Bloor, and J. W. Covell, "Determinants of myocardial hemorrhage after coronary reperfusion in

the anesthetized dog," *Circulation*, vol. 65, no. 1 I, pp. 62–69, Jan. 1982.

[77] A. R. Payne, M. Casey, J. McClure, R. McGeoch, A. Murphy, R. Woodward, A. Saul, X. Bi, S. Zuehlsdorff, K. G. Oldroyd, N. Tzemos, and C. Berry, "Bright-blood T2-weighted MRI has higher diagnostic accuracy than dark-blood short tau inversion recovery MRI for detection of acute myocardial infarction and for assessment of the ischemic area at risk and myocardial salvage," *Circ. Cardiovasc. Imaging*, vol. 4, no. 3, pp. 210–219, May 2011.

[78] N. G. Frangogiannis, C. W. Smith, and M. L. Entman, "The inflammatory response in myocardial infarction," *Cardiovasc. Res.*, vol. 53, no. 1, pp. 31–47, Jan. 2002.

[79] S. H. Choi, J. W. Kang, S. T. Kim, B. H. Lee, E. J. Chun, K. H. Schuleri, S. Il Choi, and T. H. Lim, "Investigation of T2-weighted signal intensity of infarcted myocardium and its correlation with delayed enhancement magnetic resonance imaging in a porcine model with reperfused acute myocardial infarction," *Int. J. Cardiovasc. Imaging*, vol. 25, no. SUPPL. 1, pp. 111–119, Apr. 2009.

[80] M. Westwood, L. J. Anderson, D. N. Firmin, P. D. Gatehouse, C. C. Charrier, B. Wonke, and D. J. Pennell, "A single breath-hold multiecho T2* cardiovascular magnetic resonance technique for diagnosis of myocardial iron overload," *J. Magn. Reson. Imaging*, vol. 18, no. 1, pp. 33–39, Jul. 2003.

[81] M. K. Atalay, B. P. Poncelet, H. L. Kantor, T. J. Brady, and R. M. Weisskoff, "Cardiac susceptibility artifacts arising from the heart-lung interface," *Magn. Reson. Med.*, vol. 45, no. 2, pp. 341–345, Feb. 2001.

[82] O. Bondarenko, A. M. Beek, M. B. M. Hofman, H. P. Kühl, J. W. R. Twisk, W. G. Van Dockum, C. A. Visser, and A. C. Van Rossum, "Standardizing the definition of hyperenhancement in the quantitative assessment of infarct size and myocardial viability using delayed contrast-enhanced CMR," *J. Cardiovasc. Magn. Reson.*, vol. 7, no. 2, pp. 481–485, Apr. 2005.

[83] C. Bourgault, S. Bergeron, P. Bogaty, and P. Poirier, "A most unusual acute

coronary syndrome," *Can. J. Cardiol.*, vol. 22, no. 5, pp. 429–432, Apr. 2006.

[84] M. Kosuge, T. Ebina, K. Hibi, N. Iwahashi, K. Tsukahara, M. Endo, N. Maejima, Z. Nagashima, H. Suzuki, S. Morita, S. Umemura, and K. Kimura, "Differences in Negative T Waves Between Takotsubo Cardiomyopathy and Reperfused Anterior Acute Myocardial Infarction," *Circ. J.*, vol. 76, no. 2, pp. 462–468, 2012.

[85] M. Kosuge and K. Kimura, "Clinical Implications of Electrocardiograms for Patients With Anterior Wall ST-Segment Elevation Acute Myocardial Infarction in the Interventional Era," *Circ. J.*, vol. 76, no. 1, pp. 32–40, 2012.

[86] J. C. Wood, J. M. Tyszka, S. Carson, M. D. Nelson, and T. D. Coates, "Myocardial iron loading in transfusion-dependent thalassemia and sickle cell disease," *Blood*, vol. 103, no. 5, pp. 1934–1936, Mar. 2004.

[87] V. Positano, A. Pepe, M. F. Santarelli, B. Scattini, D. De Marchi, A. Ramazzotti, G. Forni, C. Borgna-Pignatti, M. E. Lai, M. Midiri, A. Maggio, M. Lombardi, and L. Landini, "Standardized T2* map of normal human heart in vivo to correct T2* segmental artefacts," *NMR Biomed.*, vol. 20, no. 6, pp. 578–590, Oct. 2007.

[88] D. Carrick, C. Haig, S. Rauhalammi, N. Ahmed, I. Mordi, M. McEntegart, M. C. Petrie, H. Eteiba, S. Hood, S. Watkins, M. Lindsay, A. Mahrous, I. Ford, N. Tzemos, N. Sattar, P. Welsh, A. Radjenovic, K. G. Oldroyd, and C. Berry, "Prognostic significance of infarct core pathology revealed by quantitative non-contrast in comparison with contrast cardiac magnetic resonance imaging in reperfused ST-elevation myocardial infarction survivors," *Eur. Heart J.*, vol. 37, no. 13, pp. 1044–1059, Apr. 2016.

[89] J. C. Wood, C. Enriquez, N. Ghugre, J. M. Tyzka, S. Carson, M. D. Nelson, and T. D. Coates, "MRI R2 and R2* mapping accurately estimates hepatic iron concentration in transfusion-dependent thalassemia and sickle cell disease patients," *Blood*, vol. 106, no. 4, pp. 1460–1465, Aug. 2005.

[90] F. S. Prato, J. Butler, J. Sykes, L. Keenliside, K. J. Blackwood, R. T. Thompson, J. A. White, Y. Mikami, J. D. Thiessen, and G. Wisenberg, "Can the Inflammatory

Response Be Evaluated Using 18F-FDG Within Zones of Microvascular Obstruction After Myocardial Infarction?," *J. Nucl. Med.*, vol. 56, no. 2, pp. 299–304, Feb. 2015.

[91]   A. Cárdenas-Blanco, C. Tejos, P. Irarrazaval, and I. Cameron, "Noise in magnitude magnetic resonance images," *Concepts Magn. Reson. Part A Bridg. Educ. Res.*, vol. 32, no. 6, pp. 409–416, Nov. 2008.

[92]   J. Sijbers and A. J. den Dekker, "Maximum likelihood estimation of signal amplitude and noise variance from MR data," *Magn. Reson. Med.*, vol. 51, no. 3, pp. 586–594, Mar. 2004.

[93]   D. J. Pennell, "T2* magnetic resonance and myocardial iron in thalassemia," *Ann. N. Y. Acad. Sci.*, vol. 1054, no. 1, pp. 373–378, Nov. 2005.

[94]   T. W. R. A. S. CALVARD, "Picture Thresholding Using an Iterative Selection Method," *IEEE Trans. Syst. Man Cybern.*, vol. SMC-8, no. 8, pp. 630–632, 1978.

[95]   G. S. Pell, R. S. Briellmann, A. B. Waites, D. F. Abbott, and G. D. Jackson, "Voxel-based relaxometry: A new approach for analysis of T2 relaxometry changes in epilepsy," *Neuroimage*, vol. 21, no. 2, pp. 707–713, Feb. 2004.

[96]   G. S. Pell, R. S. Briellmann, A. B. Waites, D. F. Abbott, D. P. Lewis, and G. D. Jackson, "Optimized clinical T2 relaxometry with a standard CPMG sequence," *J. Magn. Reson. Imaging*, vol. 23, no. 2, pp. 248–252, Feb. 2006.

[97]   M. A. Westwood, L. J. Anderson, D. N. Firmin, P. D. Gatehouse, C. H. Lorenz, B. Wonke, and D. J. Pennell, "Interscanner Reproducibility of Cardiovascular Magnetic Resonance T2* Measurements of Tissue Iron in Thalassemia," *J. Magn. Reson. Imaging*, vol. 18, no. 5, pp. 616–620, Nov. 2003.

[98]   M. A. Tanner, T. He, M. A. Westwood, D. N. Firmin, and D. J. Pennell, "Multi-center validation of the transferability of the magnetic resonance T2* technique for the quantification of tissue iron," *Haematologica*, vol. 91, no. 10, pp. 1388–1391, Oct. 2006.

[99]   A. J. Baksi and D. J. Pennell, "T2∗imaging of the heart: Methods, applications,

and outcomes," *Top. Magn. Reson. Imaging*, vol. 23, no. 1, pp. 13–20, Feb. 2014.

[100] T. He, P. D. Gatehouse, G. C. Smith, R. H. Mohiaddin, D. J. Pennell, and D. N. Firmin, "Myocardial T*2 measurements in iron-overloaded thalassemia: An in vivo study to investigate optimal methods of quantification," *Magn. Reson. Med.*, vol. 60, no. 5, pp. 1082–1089, Nov. 2008.

[101] F. S. Prato, J. Butler, J. Sykes, L. Keenliside, K. J. Blackwood, R. T. Thompson, J. A. White, Y. Mikami, J. D. Thiessen, and G. Wisenberg, "Can the Inflammatory Response Be Evaluated Using 18F-FDG Within Zones of Microvascular Obstruction After Myocardial Infarction?," *J. Nucl. Med.*, 2015.

[102] J. D. Port and M. G. Pomper, "Quantification and minimization of magnetic susceptibility artifacts on GRE images," *J. Comput. Assist. Tomogr.*, vol. 24, no. 6, pp. 958–964, 2000.

[103] O. P. Simonetti, R. J. Kim, D. S. Fieno, H. B. Hillenbrand, E. Wu, J. M. Bundy, J. P. Finn, and R. M. Judd, "An Improved MR Imaging Technique for the Visualization of Myocardial Infarction," *Radiology*, vol. 218, no. 1, pp. 215–223, Jan. 2001.

[104] V. L. Sorrell, J. L. Anderson, P. D. Gatehouse, and R. H. Mohiaddin, "Off-frequency tuning error artifact in steady-state free precession cine imaging due to adjacent air-filled bowel," *J. Cardiovasc. Magn. Reson.*, vol. 6, no. 3, pp. 709–716, 2004.

[105] K. Kadir, H. Gao, A. Payne, J. Soraghan, and C. Berry, "LV wall segmentation using the variational level set method (LSM) with additional shape constraint for oedema quantification," *Phys. Med. Biol.*, vol. 57, no. 19, pp. 6007–6023, Oct. 2012.

[106] S. B. Reeder, A. Z. Faranesh, J. L. Boxerman, and E. R. McVeigh, "In vivo measurement of T2(*) and field inhomogeneity maps in the human heart at 1.5 T," *Magn. Reson. Med.*, vol. 39, no. 6, pp. 988–998, Jun. 1998.

[107] H. Bulluck, S. Rosmini, A. Abdel-Gadir, A. N. Bhuva, T. A. Treibel, M. Fontana,

E. Gonzalez-Lopez, M. Ramlall, A. Hamarneh, A. Sirker, A. S. Herrey, C. Manisty, D. M. Yellon, J. C. Moon, and D. J. Hausenloy, "Diagnostic performance of T1and T2mapping to detect intramyocardial hemorrhage in reperfused ST-segment elevation myocardial infarction (STEMI) patients," *J. Magn. Reson. Imaging*, vol. 46, no. 3, pp. 877–886, Sep. 2017.

[108] M. I. Zia, N. R. Ghugre, K. A. Connelly, B. H. Strauss, J. D. Sparkes, A. J. Dick, and G. A. Wright, "Characterizing myocardial edema and hemorrhage using quantitative t2 and t2* mapping at multiple time intervals post ST-segment elevation myocardial infarction," *Circ. Cardiovasc. Imaging*, vol. 5, no. 5, pp. 566–572, Sep. 2012.

[109] L. Pauling and C. D. Coryell, "The Magnetic Properties and Structure of Hemoglobin, Oxyhemoglobin and Carbonmonoxyhemoglobin," *Proc. Natl. Acad. Sci.*, vol. 22, no. 4, pp. 210–216, Apr. 1936.

[110] J. P. Carpenter, T. He, P. Kirk, M. Roughton, L. J. Anderson, S. V. De Noronha, M. N. Sheppard, J. B. Porter, J. M. Walker, J. C. Wood, R. Galanello, G. Forni, G. Catani, G. Matta, S. Fucharoen, A. Fleming, M. J. House, G. Black, D. N. Firmin, T. G. St. Pierre, and D. J. Pennell, "On T2* magnetic resonance and cardiac iron," *Circulation*, vol. 123, no. 14, pp. 1519–1528, Apr. 2011.

[111] E. Angelucci, A. Giovagnoni, G. Valeri, E. Paci, M. Ripalti, P. Muretto, C. McLaren, G. M. Brittenham, and G. Lucarelli, "Limitations of magnetic resonance imaging in measurement of hepatic iron.," *Blood*, vol. 90, no. 12, pp. 4736–42, Dec. 1997.

[112] G. M. Brittenham and D. G. Badman, "Noninvasive measurement of iron: Report of an NIDDK workshop," *Blood*, vol. 101, no. 1, pp. 15–19, Jan. 2003.

[113] P. F. Ferreira, P. D. Gatehouse, R. H. Mohiaddin, and D. N. Firmin, "Cardiovascular magnetic resonance artefacts," *J. Cardiovasc. Magn. Reson.*, vol. 15, no. 1, p. 41, 2013.

[114] P. Storey, A. A. Thompson, C. L. Carqueville, J. C. Wood, R. A. De Freitas, and

C. K. Rigsby, "R2* imaging of transfusional iron burden at 3T and comparison with 1.5T," *J. Magn. Reson. Imaging*, vol. 25, no. 3, pp. 540–547, Mar. 2007.

[115] M. Saeed, T. A. Van, R. Krug, S. W. Hetts, and M. W. Wilson, "Cardiac MR imaging: current status and future direction," *Cardiovasc Diagn Ther*, vol. 5, no. 4, pp. 290–310, Aug. 2015.

[116] N. R. Ghugre, M. Pop, R. Thomas, S. Newbigging, X. Qi, J. Barry, B. H. Strauss, and G. A. Wright, "Hemorrhage promotes inflammation and myocardial damage following acute myocardial infarction: insights from a novel preclinical model and cardiovascular magnetic resonance," *J. Cardiovasc. Magn. Reson.*, vol. 19, no. 1, p. 50, Dec. 2017.

[117] G. Wang, H. J. Yang, A. Kali, I. Cokic, R. Tang, G. Xie, Q. Yang, J. Francis, S. Li, and R. Dharmakumar, "Influence of Myocardial Hemorrhage on Staging of Reperfused Myocardial Infarctions With T2 Cardiac Magnetic Resonance Imaging: Insights Into the Dependence on Infarction Type With Ex Vivo Validation," *JACC Cardiovasc. Imaging*, Apr. 2018.

Appendix

Appendix A: on R2*, STE, and $1 - r^2$ maps, for baseline polar plots of the entire LV using, 8, 6 and 5 echoes / slice, respectively.
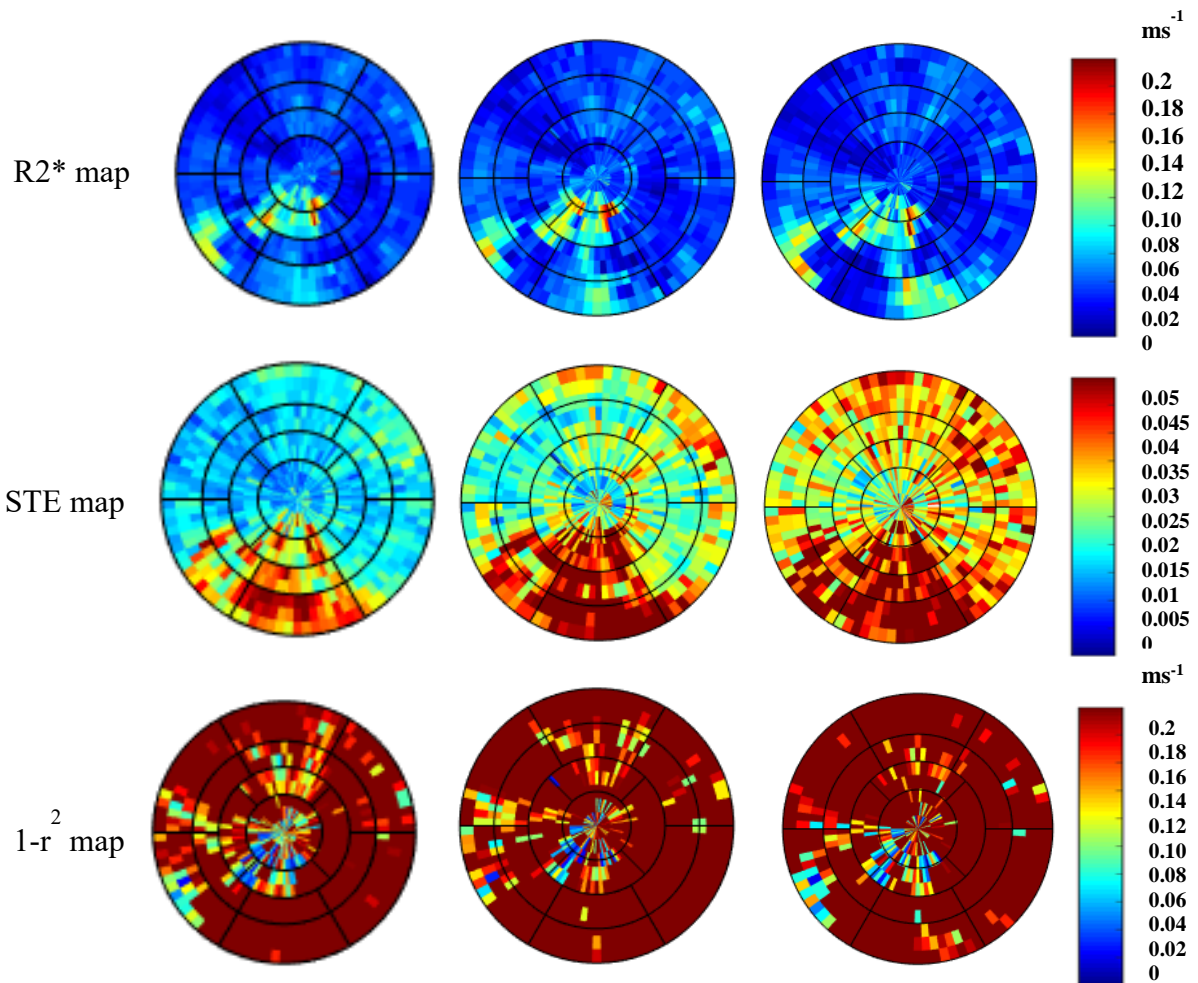
Appendix B: R2*, STE, and $1 - r^2$ maps, for baseline polar plots of the entire LV of 6 dogs using, 8/ slice
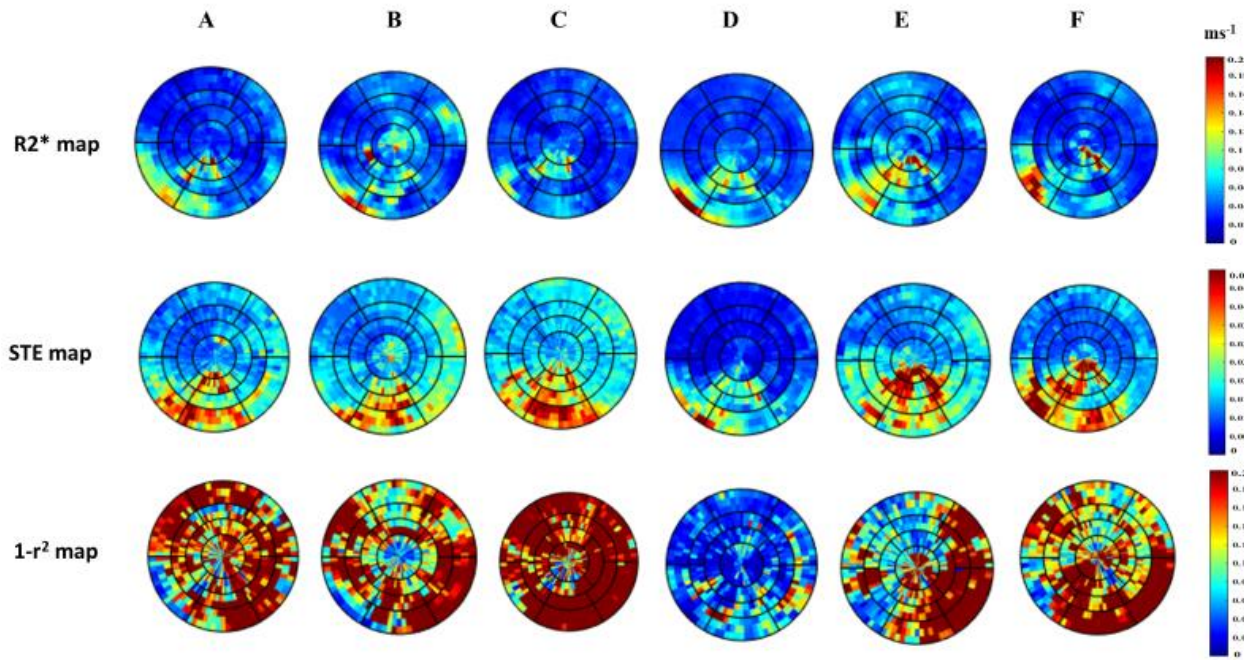
Appendix C: Ten R2* maps display short-axis slices related to apical, middle, and basal regions of the LV (right panel) and their corresponding polar plot (left panel).

R2* map

STE map

1-r² map
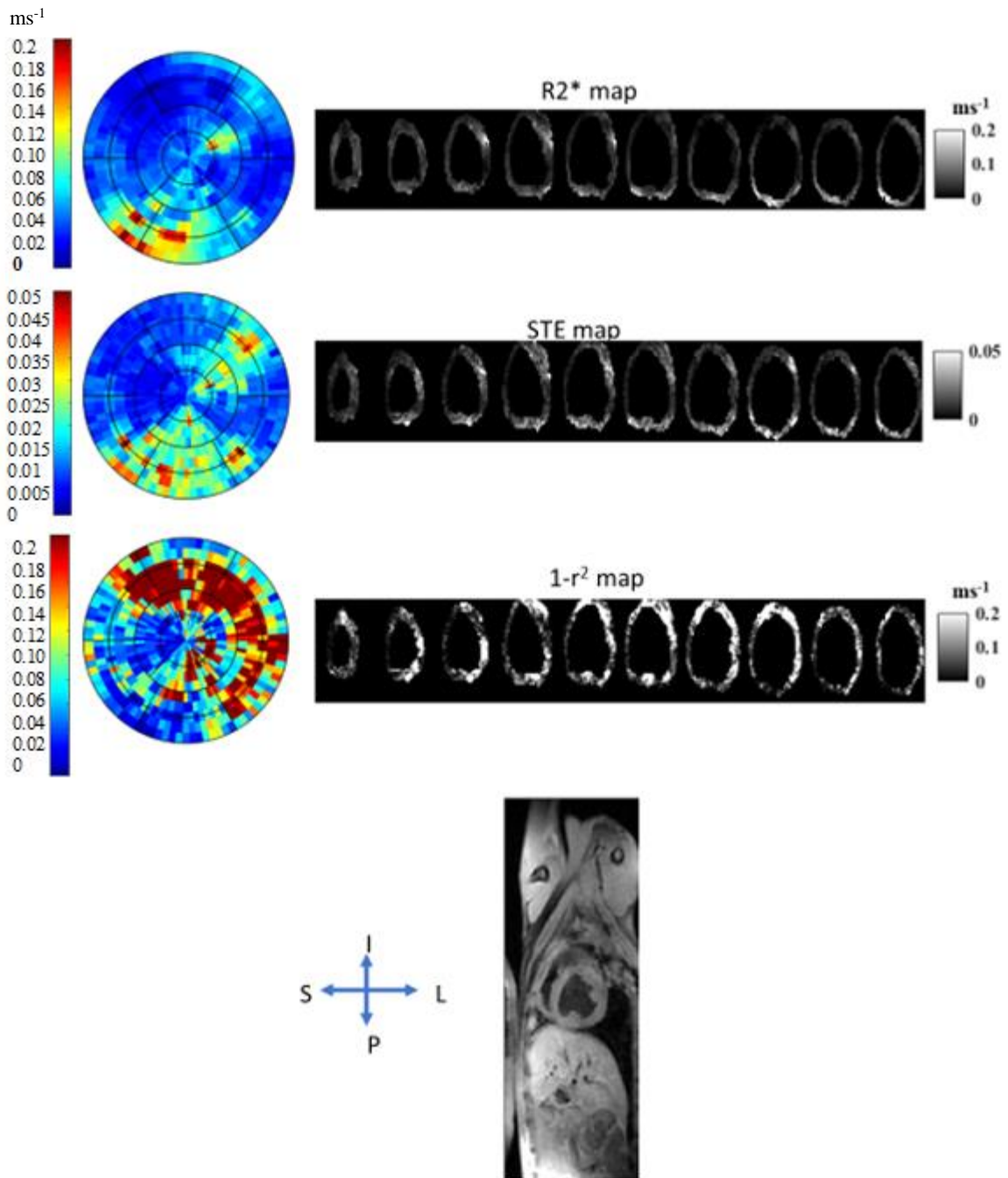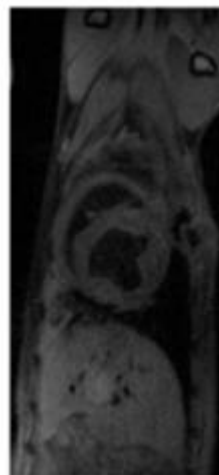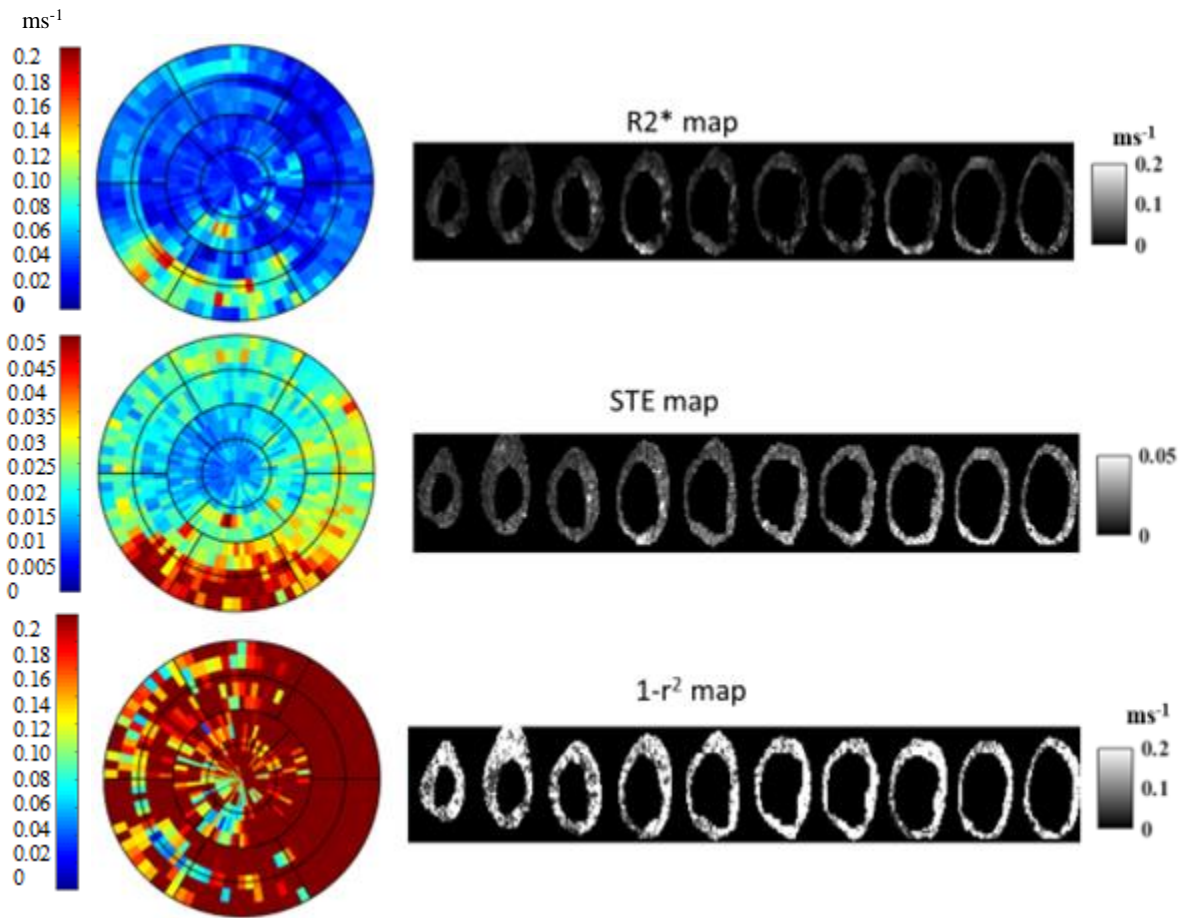
Appendix D: The distribution of R2* values within the same the uniform baseline region in six subjects

Dog 1

Dog 2

Dog 3

Dog 4

Dog 5

Dog 6
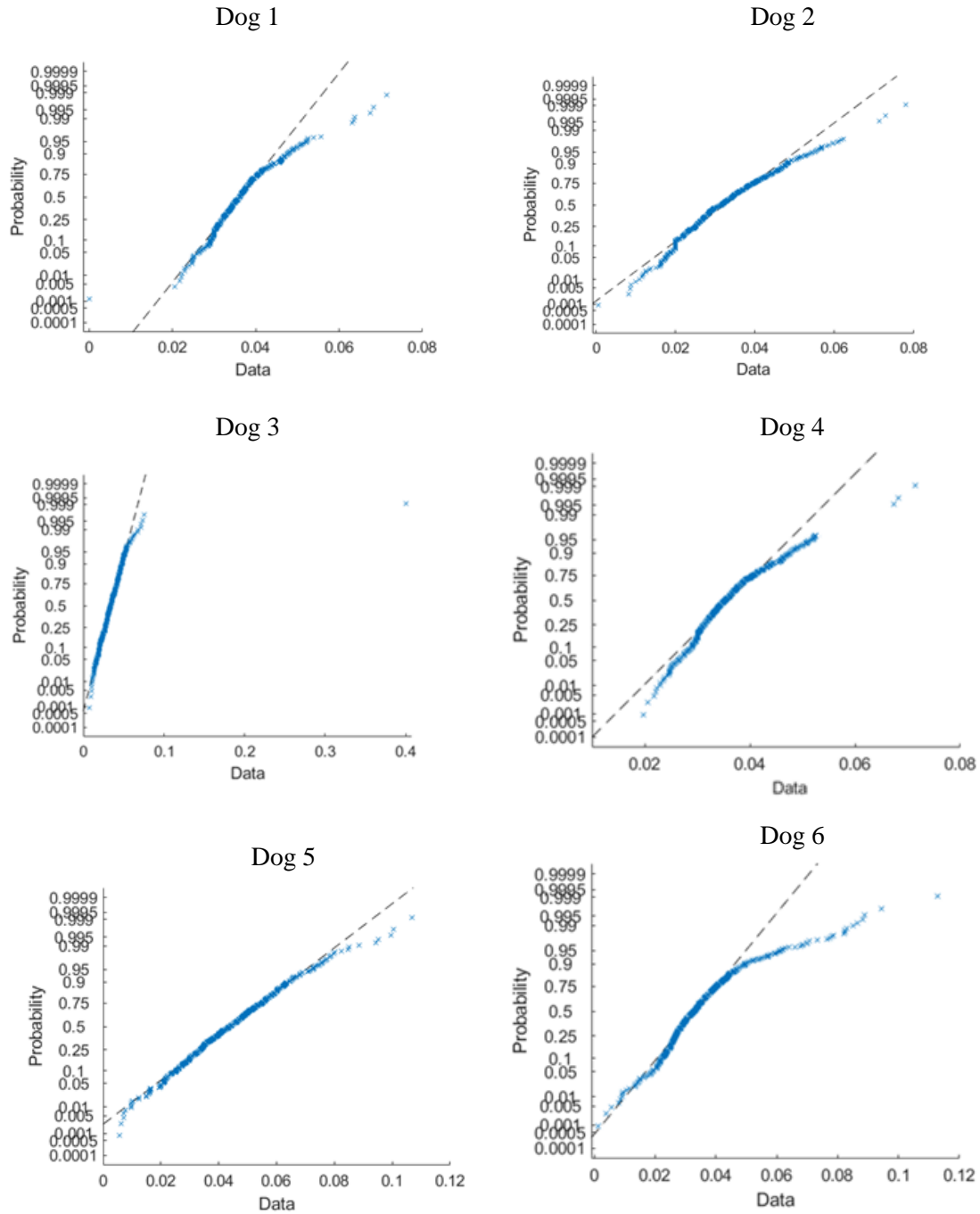
Appendix E: Polar plots represent the 17 segments of the basal, mid-ventricular and apical short-axis planes of the LV from 4 dogs, at several time-points post-MI (3,8,15,21, and 41 days)

3 days

8 days

ms^{-1}

0.2
0.18
0.16
0.14
0.12
0.10
0.08
0.06
0.04
0.02
0

15 days

21 days

41 days

3 days

8 days

15 days

21 days

41 days

ms^{-1}

0.2
0.18
0.16
0.14
0.12
0.10
0.08
0.06
0.04
0.02
0

3 days   8 days

15 days   21 days

41 days

3 days

8 days

ms^{-1}

0.2
0.18
0.16
0.14
0.12
0.10
0.08
0.06
0.04
0.02
0
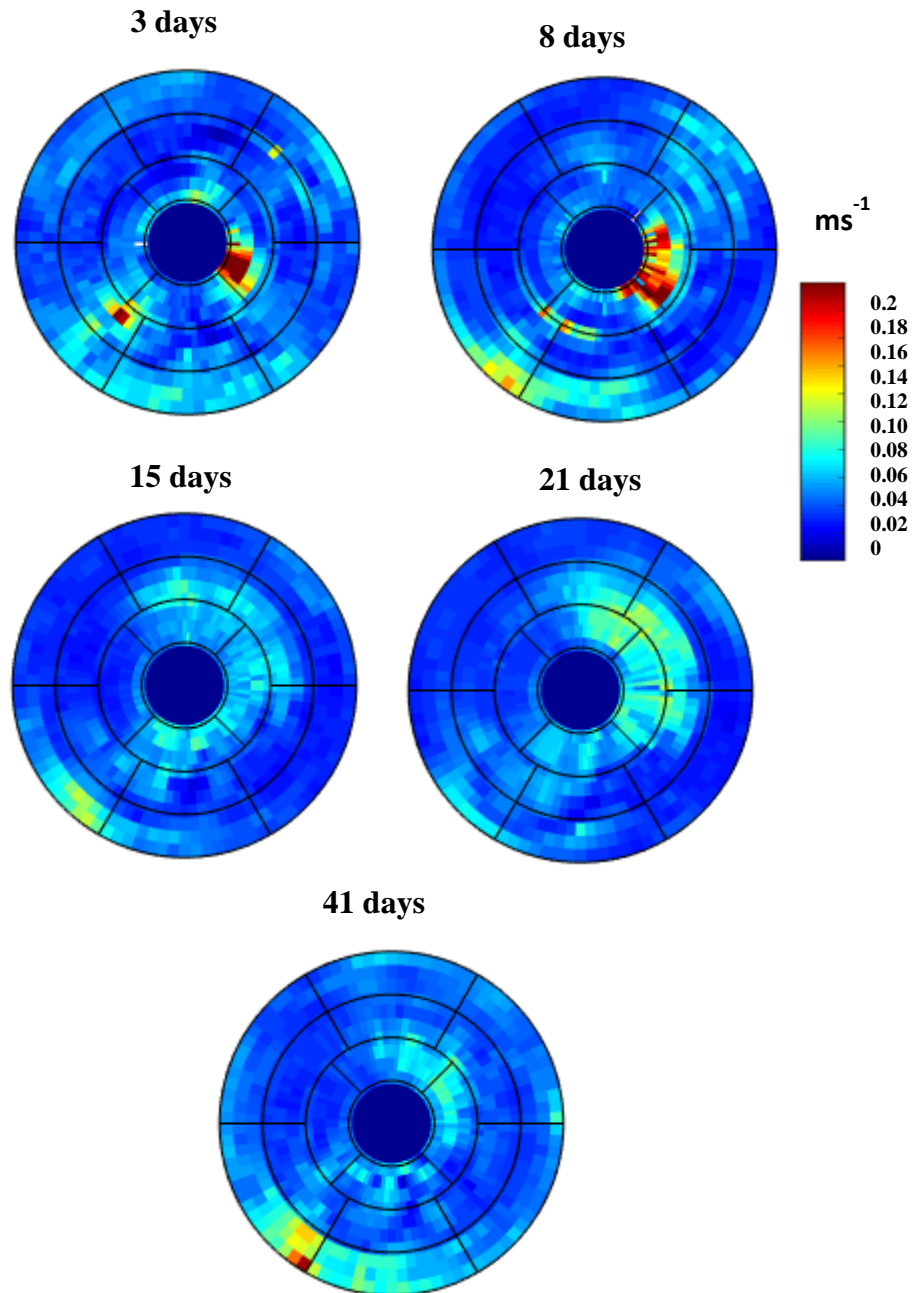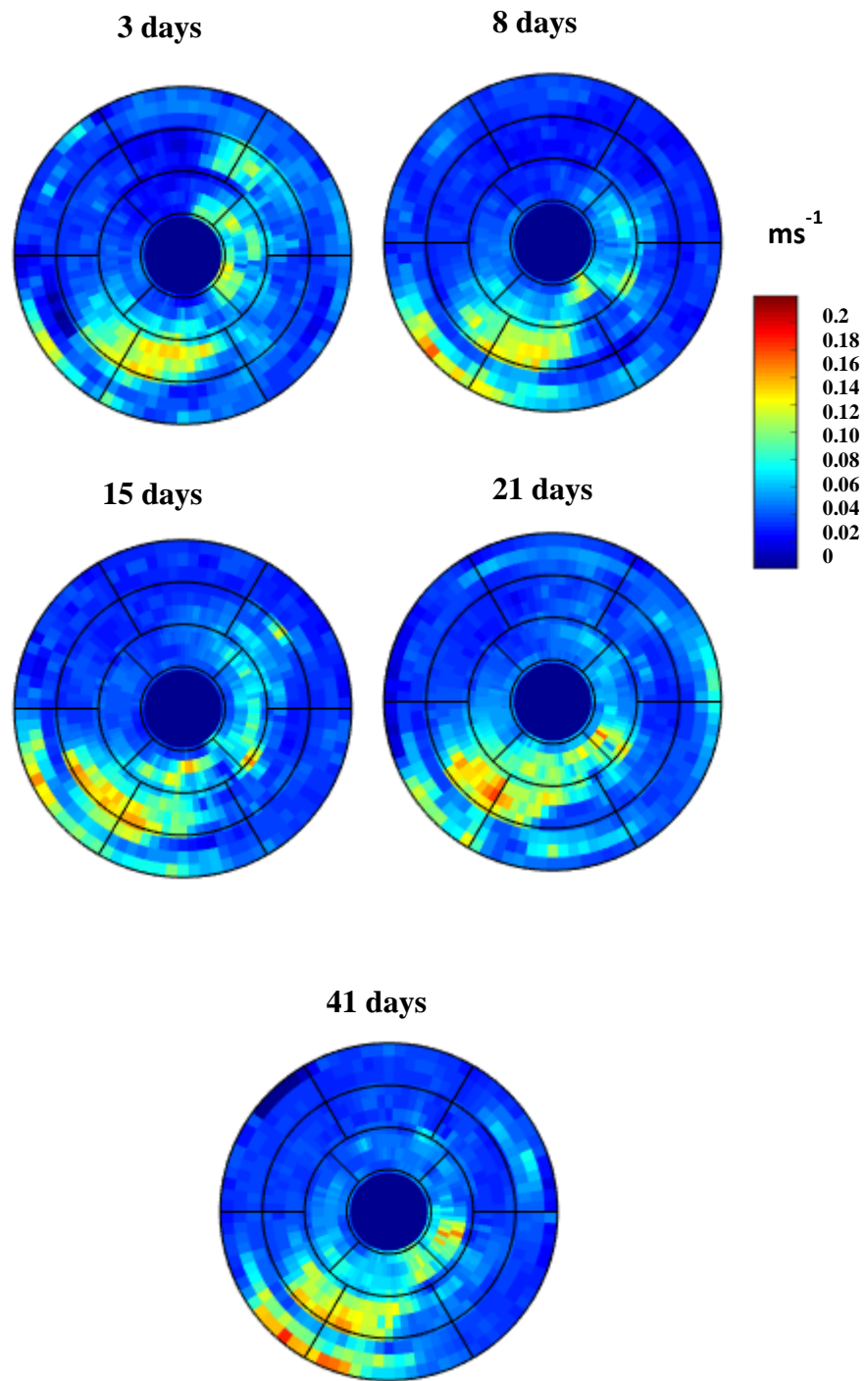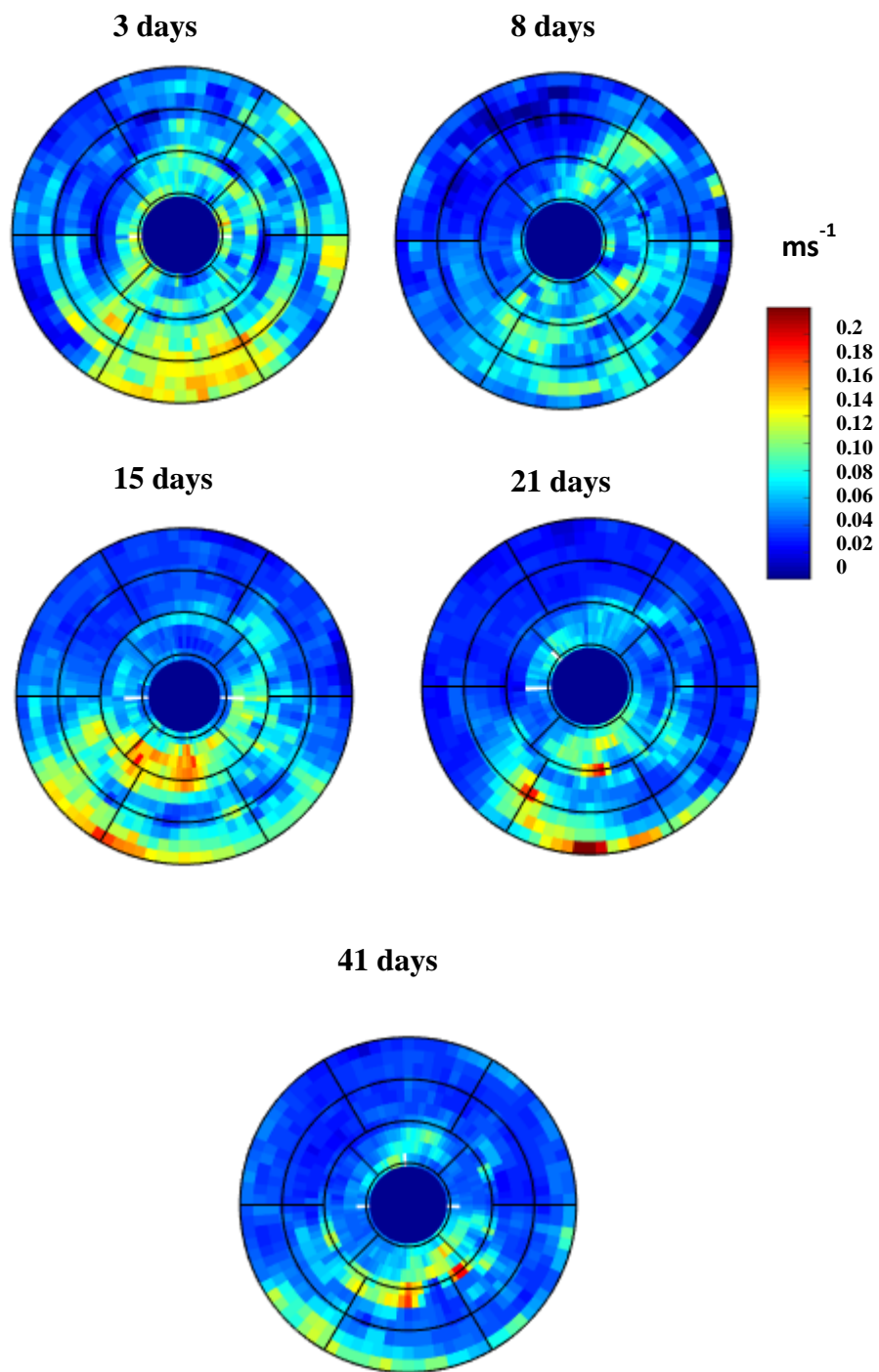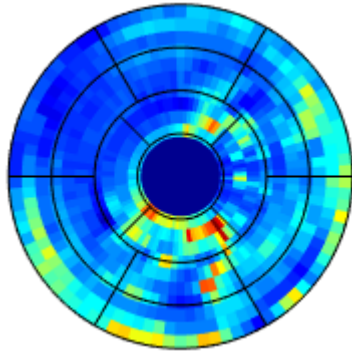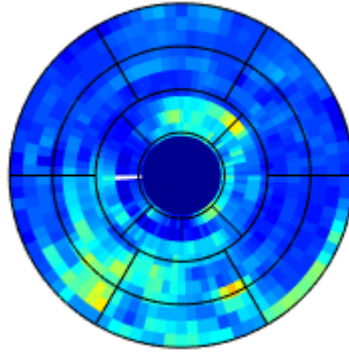
15 days
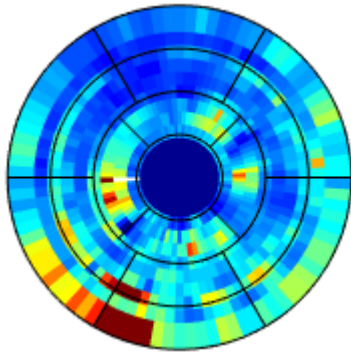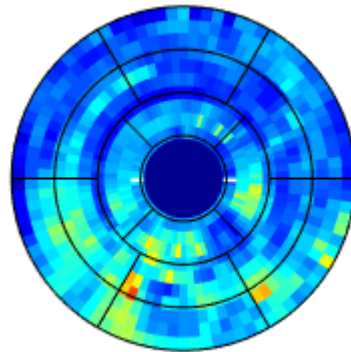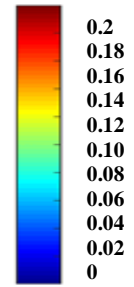
21 days

Appendix F: The non-normal R2* regions (in red) in the polar plot of the entire LV at 3,7,21, and 41 days post-MI are identified based on 0.05 and 0.08 ms^{-1} thresholds for dogs 1-4 (in order).
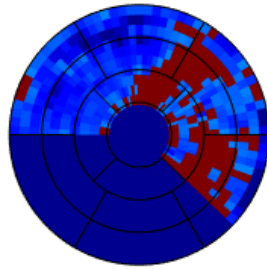

0.05 ms^{-1}   **0.08 ms^{-1}**

Day 7

Day 15
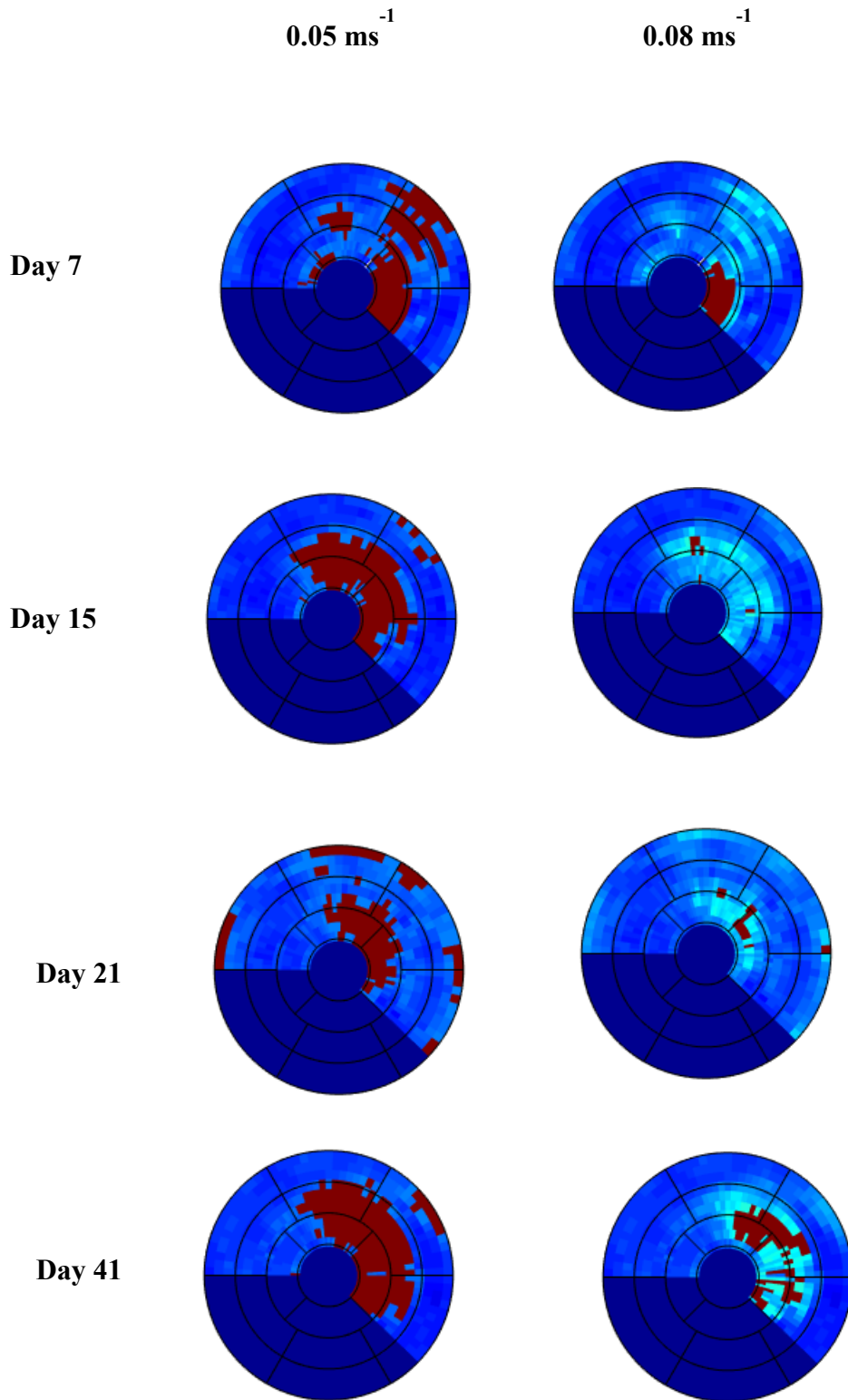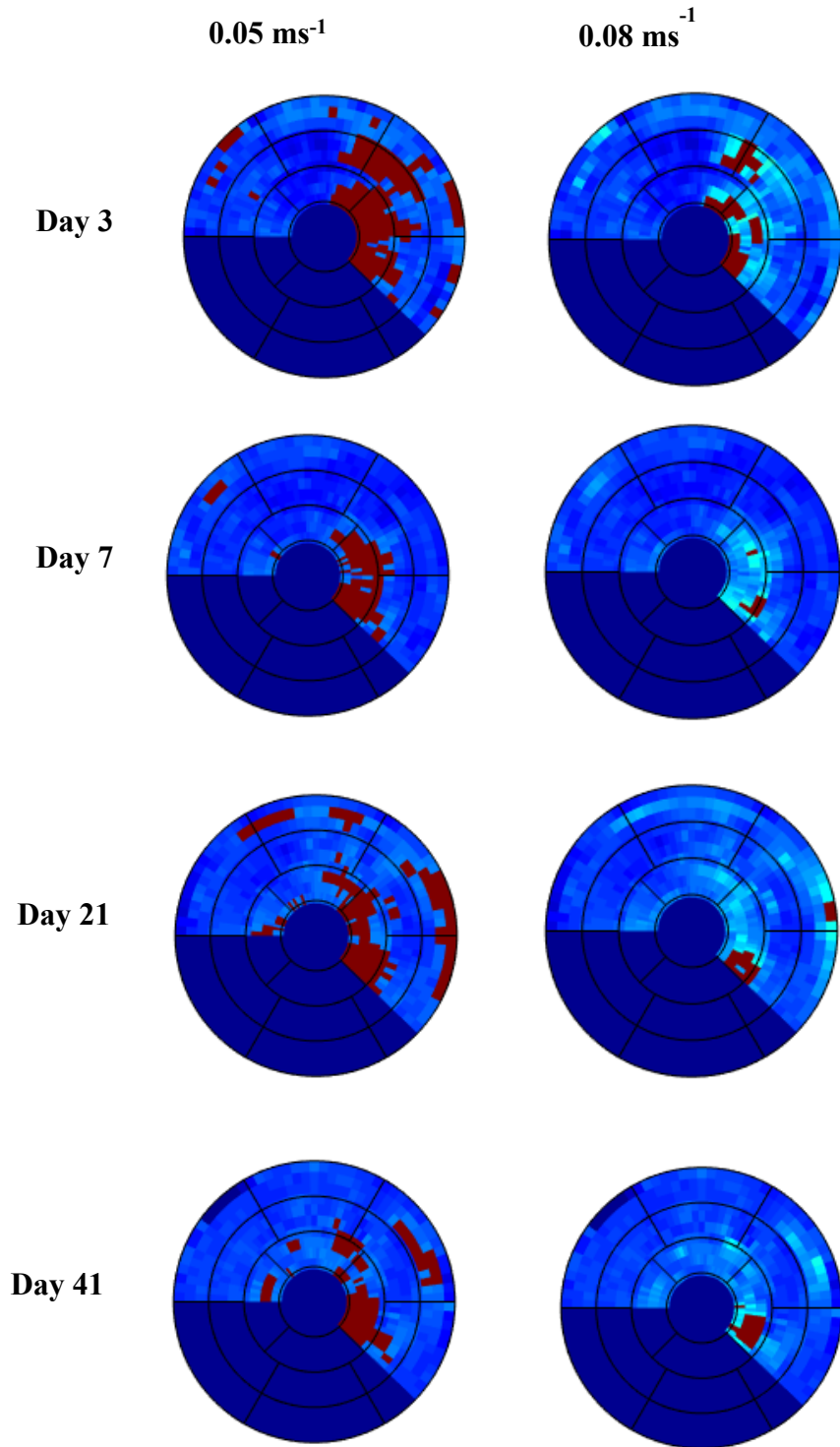
Day 21

Day 41

0.05 ms⁻¹   0.08 ms⁻¹

Day 3
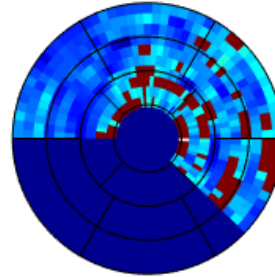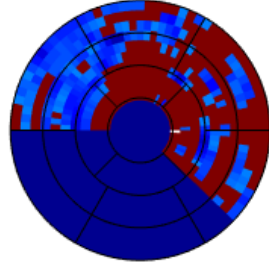
Day 7
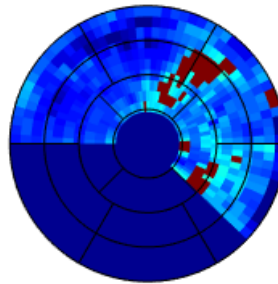
Day 21
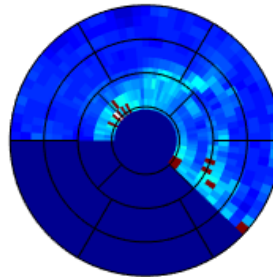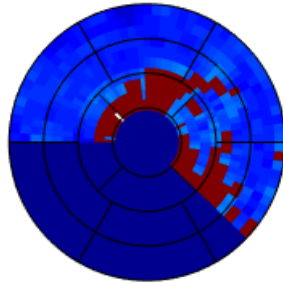
Day 41
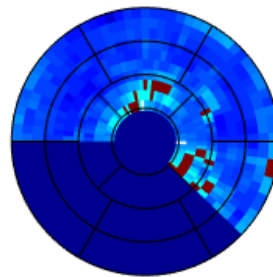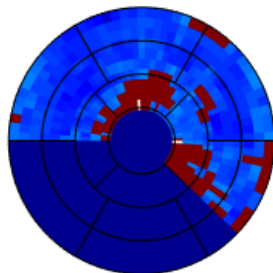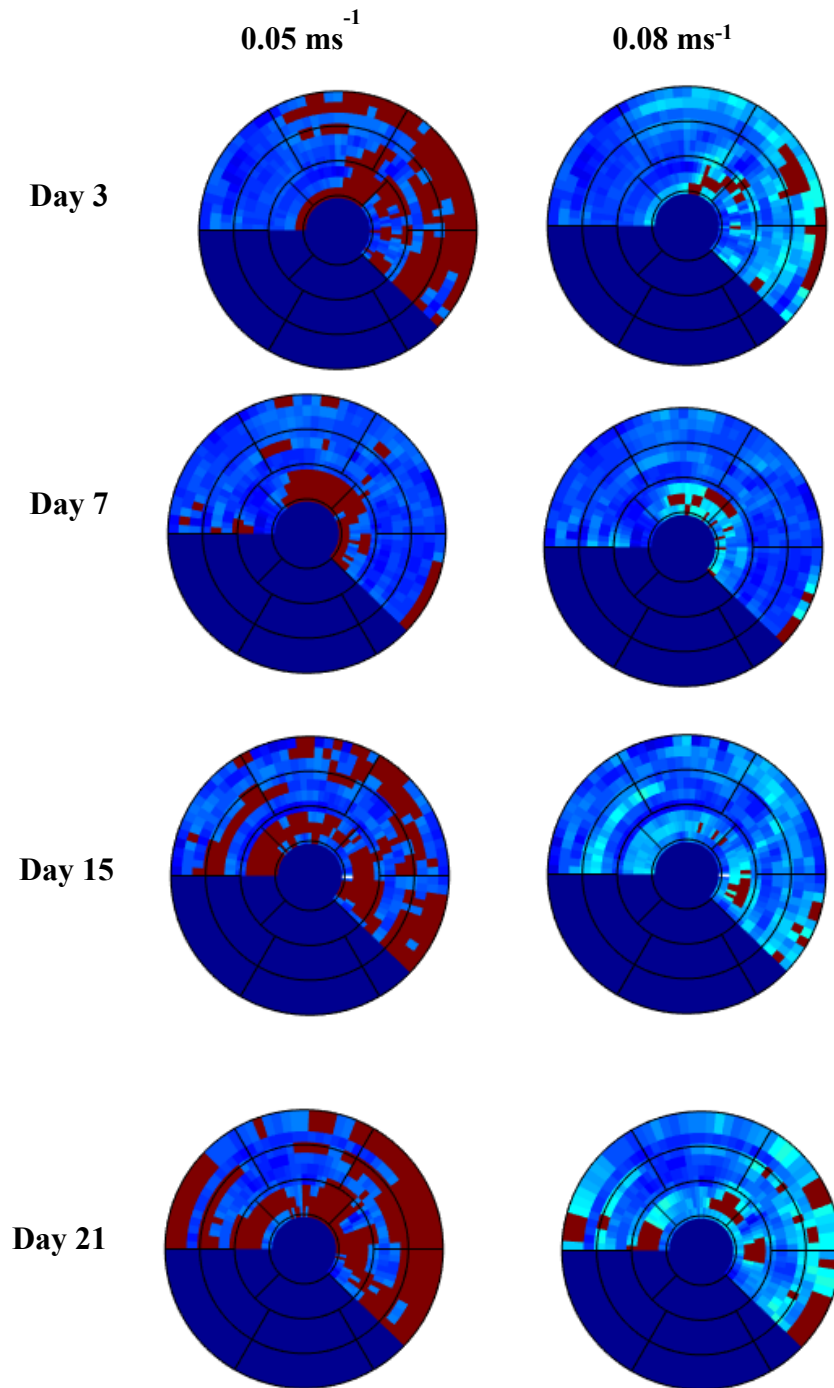
Curriculum Vitae

Name:	Khalid Abdalla
Education:	M.Sc. Candidate, Medical Biophysics
	Western University, London, ON
	2017-present
	M.Sc. Medical Physics
	KFUPM, Dhahran, Saudi Arabia
	2004-2006
	B.Sc. Physics
	Mut'ah university, Karak, Jordan
	1992-1996
Appointments:	Physics Lecturer
	University of Hail, Hail, Saudi Arabia
	2007-2015

Conferences:

Abstracts-Posters:

- **Abdalla** *et al.* Analyzing myocardial R2* mapping post myocardial infarction using stabilized probability plots. World Molecular Imaging Congress (WMIC), Seattle, USA, September 2018.

- **Abdalla** *et al.* Detecting myocardial hemorrhage with R2* maps. Imaging Network Ontario (ImNO), London, Ontario, March 2018.

- **Abdalla** *et al.* Analysis of Myocardial Hemorrhage on MR Images: Segmentation of Short T2* Regions Using K-Means Clustering. London Imaging Discovery Day, London, Ontario. 2017.